Revision 1

Chemical and boron isotopic composition of tourmaline from the Yixingzhai gold deposit, North China Craton: Proxies for ore fluids evolution and mineral exploration

Shao-Rui Zhao[1,2], Hao Hu[1], Xiao-Ye Jin[1,2*], Xiao-Dong Deng[1], Paul T. Robinson[1,2], Wen-Sheng Gao[2], Li-Zhong Zhang[2,3]

[1] State Key Laboratory of Geological Processes and Mineral Resources, China University of Geosciences, Wuhan 430074, China

[2] School of Earth Resources, China University of Geosciences, Wuhan 430074, China

[3] Mineral Exploration Institute, Zijin Mining Group Co., Ltd., Xiamen 361006, China

*Corresponding author:

E-mail: xiaoye.jin@cug.edu.cn

Phone: +86 180 8640 0086

Fax: +86 27 6788 3051

ABSTRACT

Tourmaline is common in magmatic-hydrothermal deposits, and its composition and boron isotope geochemistry have been widely used to fingerprint the source and evolution of hydrothermal fluids and associated metals. However, whether these chemical or boron isotopic compositions or their combinations can be used as vectors for mineral exploration remains to be explored. In this study, we documented the major and trace element compositions and boron isotopic values of tourmaline along a vertical extension (i.e., 510, 830, 1230 m above sea level) of the newly discovered porphyry Au mineralization in the Hewan feldspar quartz porphyry, Yixingzhai deposit, to shed light on the evolution of the ore-forming fluid, the mechanisms of Au deposition, and potential indicators for Au exploration. Field observations showed that tourmaline in the Hewan porphyry occurred mainly as orbicules or veins, and intergrew with Au-bearing pyrite, hydrothermal quartz, and some clay minerals, indicating a magmatic-hydrothermal origin. Tourmaline sampled from the 510 m above sea level showed $\delta^{11}B$ values (-11.5 to -9.3‰) consistent with those of the average continental crust and tourmaline in magmatic systems, which suggests that the ore-forming fluid was most likely exsolved from the host Hewan porphyry. The $\delta^{11}B$ values became heavier upward, reaching -9.9 to -1.5‰ at 830 m and -8.0 to +6.8‰ at 1230 m above sea level. This boron isotopic variation, integrated with increasing Fe, Mg, Na, Ca, Li, Co, and Sr but decreasing Al, U, Th, REE, Zn, and Pb contents of the tourmaline samples from deep to shallow levels, implies that the initial magmatic fluids were gradually mixed with circulating meteoric water that contained

materials leached from peripheral Archean metamorphic rocks and Mesoproterozoic marine sedimentary rocks. Considering the spatial distribution of the Au grade of the porphyry, we propose that a suitable mixing proportion of magmatic and meteoric fluids caused Au deposition and accumulation. We note that tourmaline samples collected from the economic Au zones had much lower and more concentrated $\delta^{11}B$ (-11.5 to -3.0‰), Co/(Pb+Zn) (<0.01), and Sr/(Pb+Zn) (0.27 to 1.07) values than those in low-grade or barren zones. Coeval plutons and breccia pipes, where tourmaline also occurs, are well developed inside and outside the Yixingzhai Au mine. We suggest that the obtained parameters can potentially be used as proxies for further Au exploration in this region. This study highlights the feasibility of using the chemical and isotopic compositions of tourmaline for mineral exploration.

Keywords: Tourmaline geochemistry; Fluid evolution; Mineral exploration; Yixingzhai Au deposit; North China Craton

INTRODUCTION

Tourmaline is a common mineral in various hydrothermal ore deposits, especially in granitoid-related magmatic-hydrothermal deposits (e.g., Jiang et al. 2008; Dutrow and Henry 2011; Slack and Trumbull 2011; Sciuba et al. 2021). As tourmaline is stable over a wide range of temperatures and pressures and has extremely low rates of volume diffusion and high resistance to metasomatic alteration

(Dutrow and Henry 2011), its microtextures, major-trace elements, and boron isotopes have been used to trace magmatic and hydrothermal processes in selected ore deposits (Slack and Trumbull 2011; van Hinsberg et al. 2011). Recent studies have also shown that its chemical and isotopic characteristics can provide insights into the mechanisms causing the associated mineral deposition (e.g., Harlaux et al. 2021; Zhao H.D. et al. 2021), suggesting that tourmaline could be used as a guide in ore deposit exploration (e.g., Arif et al. 2010; Sciuba et al. 2021).

The Yixingzhai Au deposit in the north-central part of the North China Craton (NCC) has been explored and mined for nearly half a century (28 t Au @ 10–20 g/t; He 2014; Li et al. 2014). Recent exploration has recognized that Hewan porphyry in the mining area is wholly mineralized, with a proven reserve of >50 t Au at an average grade of 2.3 g/t (Zhang 2018). The relevant mineralization features have been well documented and show many similarities to porphyry Au deposits (e.g., Zhang 2018; Zhang et al. 2020), but the evolution of ore-forming fluids and mechanisms for Au deposition remain unclear. Whether the numerous coeval plutons and cryptoexplosive breccia pipes in the mine area host similar gold mineralization remains unknown. Tourmaline is widespread in the mineralized Hewan porphyry and other plutons/pipes in the Yixingzhai mine. In the Hewan porphyry, tourmaline is spatially related to Au-bearing pyrite, hydrothermal quartz, and sericite. These observations make tourmaline an ideal candidate to fingerprint hydrothermal fluid evolution, to understand Au deposition, and potentially to assist in regional Au exploration.

In this paper, we presented a detailed textural, chemical, and boron isotope study of tourmaline in the Hewan porphyry to provide new insights into Au mineralization. The petrographic and textural features of tourmaline were presented to confirm its hydrothermal origin. The in-situ major-trace element contents and boron isotope values were then used to trace the evolution of ore-forming fluids and investigate various mechanisms of Au deposition. Finally, the feasibility of using the chemical and boron isotopic compositions of tourmaline as guides for further Au exploration was discussed.

GEOLOGICAL BACKGROUND

The Yixingzhai Au deposit is located in the north-central domain of the Trans-North China Orogen (TNCO) of the NCC, which was formed by the collision and amalgamation of the Eastern and Western Blocks in the late Paleoproterozoic (Fig. 1A; Zhao et al. 2005; Zhai 2011). This region is dominated by Archean metamorphic rocks, mainly tonalite-trondhjemite-granodiorite gneiss, with minor amounts of amphibolite and granulite. The protoliths of these rocks are mafic to felsic volcanic rocks interlayered with clastic rocks, all of which were metamorphosed to greenschist or amphibolite facies rocks during the formation of the TNCO (Wei 2018). These metamorphic rocks are locally overlain by Mesoproterozoic dolomites and marbles (Fig. 1B) and locally preset marine evaporites. The Precambrian rocks are intruded, from southeast to northwest, by the Sunzhuang diorite (zircon U-Pb ages of 139 ± 1 to

134 ± 1 Ma; Li et al. 2014; Zhang et al. 2015), the Nanmenshan quartz porphyry (141 ± 1 Ma; Zhang et al. 2020), and the Hewan feldspar quartz porphyry (141 ± 1 Ma; Zhang 2018). It is noted that the Mesoproterozoic carbonate rocks are locally enclosed in the Early Cretaceous intrusions and have experienced skarn alteration (Fig. 1B). Numerous dikes, including diabase, felsite, and lamprophyre, have intruded into the mining area (Fig. 1B). They are thought to have formed at two discrete ages: the Paleoproterozoic and Early Cretaceous (Zhang 2018). The structures in the Yixingzhai mine are predominantly NW- and minor NS-trending faults, along with four cryptoexplosive breccia pipes, Tietangdong, Jinjiling, Nanmenshan, and Hewan, in the mining area (Fig. 1B). Garnet and zircon U-Pb dating have constrained the timing of these four breccia pipes to approximately 140 Ma (Zhang et al. 2020).

Gold mineralization in the Hewan porphyry is characterized by interspersed pyrite disseminations and quartz-pyrite veinlets or stockworks that transect the porphyry. Relatively high-grade Au ores (>1.0 g/t) are mainly present between 500 and 1100 m above sea level (a.s.l.; Fig. 2). The ore minerals are mostly pyrite with minor amounts of chalcopyrite, sphalerite, galena, molybdenite, tetrahedrite, covellite, magnetite, and hematite. Gold occurs mainly as native Au or as electrum enclosed in pyrite (Zhang 2018). Gold mineralization is widely accompanied by potassium silicate and intermediate argillic alteration. Potassium silicate alteration is best developed below ~ 400 m a.s.l. and consists mainly of K-feldspar. This mineral assemblage is present in the form of dissemination, veinlets, and matrix flooding. Quartz, magnetite, and molybdenite veinlets are common in the K-silicate alteration zone. Intermediate

128 argillic alteration is a term used by Vila and Sillitoe (1991) to describe the mineral
129 assemblage of quartz-sericite-chlorite-smectite, which is accompanied by quartz
130 veinlets, pyrite, and magnetite/hematite in the Hewan porphyry. However, the
131 development of intermediate argillic alterations does not always indicate a high Au
132 grade. Potassium silicate assemblages are locally observed in and are commonly
133 overprinted by intermediate argillic alteration. Both the K silicate and intermediate
134 argillic alteration zones are transitional outward and upward to the propylitic and
135 advanced argillic alteration zones, characterized mainly by chlorite-calcite-epidote
136 and kaolinite-alunite assemblages, respectively. These two alteration zones are
137 characterized by low-grade Au mineralization. Molybdenite Re-Os dating, coupled
138 with garnet and zircon U-Pb dating, suggests that Au mineralization in the Hewan
139 porphyry occurred at ca. 140 Ma (Zhang et al. 2017, 2020), coeval with the
140 emplacement of the host porphyry and formation of breccia pipes.
141

142 ## TOURMALINE OCCURRENCES

143 Field observations and drill-core logging showed that tourmaline was present
144 from the surface to a depth of approximately 700 m in the Hewan porphyry (Fig. 2).
145 The occurrences, morphologies, textures, and mineral associations of tourmaline at
146 different levels are summarized in Table 1 and described in detail here. In the deep
147 parts (e.g., 510 m a.s.l.; Fig. 2), tiny tourmaline particles, chiefly along with quartz,
148 formed small orbicular clusters that were disseminated in the mineralized porphyry

149 (Fig. 3A). The tourmaline grains were mostly scattered in the cores of the orbicules
150 with no observed orientation (Fig. 3B), interspersed with leucocratic minerals in the
151 mantles, or clustered along the rims of the orbicules (Fig. 3C). In the latter case,
152 tourmaline crystals commonly grew unidirectionally from the matrix towards the
153 pyrite in the cores of the orbicules (Fig. 3C). Individual tourmaline crystals occurred
154 as euhedral to anhedral columns, with grain sizes varying from 20 × 50 to 50 × 200
155 μm. These grains were easily recognized by their pleochroism from light yellow to
156 dark blue (Fig. 3B, C). Tourmaline in the orbicules coexisted spatially with pyrite,
157 sericite, quartz, chlorite, and smectite (Fig. 3B–E). Some quartz grains contained
158 assemblages consisting of single-phase liquid, two-phase liquid-vapor, and three-
159 phase halite-bearing fluid inclusions (Fig. 3D). In the back-scattered electron (BSE)
160 images, the tourmaline grains showed slightly strip-like textures (Fig. 3E).

161 Two types of tourmalines were identified in the middle parts of the Hewan
162 porphyry (e.g., 830 m a.s.l.; Fig. 2). The first type occurred as orbicules or patches,
163 generally 0.5 to 2 cm across, that were texturally associated with quartz and pyrite
164 (Fig. 4A). The second type formed tourmaline-quartz-pyrite veins that transected the
165 porphyry (Fig. 4B). These veins with variable lengths were mostly 5–10 cm wide and
166 generally tailed out into the host porphyry where they formed structurally isolated
167 entities. Both types typically formed columnar to lenticular tourmaline grains with
168 variable lengths of 100 to 1000 μm (Fig. 4A–D). In the thin sections, some tourmaline
169 aggregates were rimmed by leucocratic halos, which were mainly composed of fine-
170 grained quartz and sericite, with or without chlorite, smectite, and feldspar (Fig. 4C).

These tourmaline grains showed a different pleochroism, from yellowish-brown to greenish-brown (Fig. 4C, D). Quartz intergrown with tourmaline contained abundant vapor-liquid and vapor-liquid-halite fluid inclusions (Fig. 4E). In the BSE images, tourmaline generally exhibited patchy zones and was intimately intergrown with pyrite and quartz (Fig. 4F).

In the shallow parts of the Hewan porphyry (e.g., 1230 m a.s.l.; Fig. 2), tourmaline mainly occurred as large orbicules with diameters ranging from 0.5 to 4 cm (Fig. 5A, B). These orbicules generally consisted of quartz and tourmaline that were surrounded by leucocratic halos with a width of 0.1–0.5 cm (Fig. 5B). The leucocratic halos were mineralogically dominated by kaolinite, alunite, sericite, quartz, and/or feldspar (Fig. 5B). Tourmaline crystals in these orbicules were euhedral to subhedral, 200–1500 μm in size, and exhibited pleochroism from yellowish green to dark greenish brown (Fig. 5C, D). They were typically interstitial with quartz crystals (Fig. 5C, D). In addition, tiny tourmaline and pyrite grains were observed as mineral inclusions encapsulated along the quartz growth zones (Fig. 5D, F). The fluid inclusion assemblages in the quartz were similar to those in the samples from 510 and 830 m a.s.l. and mainly included two-phase liquid-vapor fluid inclusions with variable vapor/liquid ratios and halite-bearing three-phase fluid inclusions (Fig. 5E). In the BSE images, the tourmaline grains showed well-developed oscillatory zoning and contained numerous tiny quartz inclusions (e.g., Fig. 5F).

SAMPLES AND ANALYTICAL METHODS

193 Samples collected from an outcrop at ~ 1230 m a.s.l., an 830-m adit, and an
194 underground drill core ZK602F at 510 m a.s.l. were investigated for textural studies
195 (Fig. 2). The samples were prepared as standard thin sections and examined
196 successively using an optical microscope under reflected and transmitted light and a
197 scanning electron microscope (SEM) equipped with an energy-dispersive
198 spectrometer (EDS). The operational conditions for SEM-EDS were set at an
199 accelerating voltage of 20 kV and beam size of 5 μm. Subsequently, the areas of
200 interest were selected for major (n = 102), trace (n = 53), and boron isotopic (n = 105)
201 analyses.

202 The major elemental composition of tourmaline was analyzed using a JEOL
203 JXA-8230 Electron Probe Microanalyzer (EPMA) with four wavelength-dispersive
204 spectrometers at the Center for Global Tectonics, School of Earth Sciences, China
205 University of Geosciences (Wuhan). An accelerating voltage of 20 kV, a beam current
206 of 20 nA, and a beam diameter of 1 μm were used for all the analyses. The dwell
207 times were 10 s for the elemental peaks and 5 s for the background locations adjacent
208 to the peaks. The following reference standards were used for calibration: SiO_2 (Si),
209 TiO_2 (Ti), $NaAlSi_3O_8$ (Na and Al), Fe_2O_3 (Fe), $MnSiO_3$ (Mn), $(Mg, Fe)_2SiO_4$ (Mg),
210 $CaCO_3$ (Ca), and $KAlSi_3O_8$ (K). The data were reduced online using the conventional
211 ZAF routine. The analytical precision was >1% for elements with concentrations
212 higher than 5 wt. %, and better than 5% for elements with contents at 0.01–5 wt. %.
213 The structural formulae of tourmaline were calculated by normalizing to a sum of 15
214 cations in the octahedral and tetrahedral sites (T + Z + Y) following the method of

Henry et al. (2011). The proportion of X site vacancies was calculated as [1 - (Na + Ca + K)]. The B_2O_3 and H_2O contents were calculated from stoichiometric constraints, assuming B = 3 atoms per formula unit (a.p.f.u.) and OH^- = 3.5 a.p.f.u. Mineral formulae were calculated assuming 31 total anions (O^{2-} and OH^-). The $Fe^{3+}/(Fe^{3+}+Fe^{2+})$ values of the tourmaline were estimated using the method described by Jiang et al. (2008). Despite the large uncertainties in the estimates, it has been shown to be useful in recording the relative oxidative-reductive conditions for successive tourmaline formations (Jiang et al. 2008; Zhao H.D. et al. 2021).

The trace elemental compositions of the tourmaline were determined by laser ablation inductively coupled plasma mass spectrometry (LA-ICP-MS) at the State Key Laboratory of Geological Processes and Mineral Resources (GPMR), China University of Geosciences (Wuhan). A GeoLas 2005 laser ablation system coupled with an Agilent 7700 ICP-MS instrument was used. Laser sampling was performed with a spot size of 44 μm. A "wire" signal smoothing device was included in this laser ablation system, by which smooth signals were produced even at very low laser repetition rates down to 1 Hz (Hu et al. 2012). Helium (~400 ml/min) was used as the carrier gas and mixed with argon (~800 ml/min) before entering the ICP system. A small amount of nitrogen (4 ml/min) was added to the central gas flow to enhance sensitivity, improve precision, and lower detection limit. Each analysis incorporated a background acquisition of approximately 20–30 s (gas blank), followed by 50 s of data acquisition from the sample. The data were calibrated against multiple reference standards: BIR-1G, BCR-2G, BHVO-2G, and SRM610. Raw data reduction was

performed offline using ICPMSDataCal software (Liu et al. 2008), and quantitative calibration was performed using the method described by Chen et al. (2014). The analytical precision for most elements was estimated to be better than 10%.

The boron isotopes of tourmaline were analyzed using a RESOlution S-155 laser ablation system coupled to a Nu Plasma II multi-collector ICP-MS (LA-MC-ICP-MS) at the GPMR. The analyses were performed using a 50-μm-diameter spot with a laser fluence of 4 J/cm^2 and a repetition frequency of 10 Hz. The isotopic signals of ^{10}B and ^{11}B were simultaneously acquired using two Faraday cups. The mass bias of the instrument was calibrated using the standard-sample-standard bracketing method. An international tourmaline standard IAEA B4 (δ^{11}B = -8.71‰; Tonarini et al. 2003) was used for external calibration. Two other tourmaline reference materials, schorl (HS#112566) and dravite (HS#108796) from the Harvard Mineralogical Museum (Dyar et al. 2001), were used to assess the analytical quality. The external precision (2σ) is estimated to be better than 0.5‰ based on replicate analyses of the reference tourmalines. The internal precision (1SD) in per mil for a single analysis was calculated from approximately 100 cycles of each analysis (Zhao K.D. et al. 2021).

RESULTS

Major elemental compositions

The major elemental compositions and structural formulae of the tourmaline samples are listed in Supplementary Table A1 and graphically illustrated in Figure 6.

Tourmaline samples from the different levels shared comparable SiO_2 (33.15–37.04%), $B_2O_{3cal.}$ (9.71–10.54%), and $H_2O_{cal.}$ (2.93–3.18%) concentrations (Fig. 6). However, notable variations were observed in the abundances of other oxides from the deep to shallow parts of the Hewan porphyry. For example, the median concentrations of FeO, MgO, Na_2O, and CaO in the tourmaline gradually increased from 510 to 1230 m a.s.l. (Fig. 6; Supplementary Table A1). In contrast, the Al_2O_3 and K_2O concentrations of the tourmaline samples decreased from 510 to 1230 m a.s.l. (Fig. 6; Supplementary Table A1). The median concentrations of TiO_2 and MnO in tourmaline showed more varied depth patterns, i.e., both increased from 510 to 830 m a.s.l. and then decreased to 1230 m a.s.l. (Fig. 6; Supplementary Table A1). Tourmaline samples from 510 m a.s.l. yielded $Fe^{3+}/(Fe^{3+}+Fe^{2+})$ values of 0–0.16 (with a mean of 0.06). These values increased to 0–0.63 (mean = 0.17) and 0.16–0.80 (mean = 0.33) for tourmaline samples from 830 and 1230 m a.s.l., respectively (Supplementary Table A1).

According to the classification by Henry et al. (2011), the studied tourmaline samples mostly belonged to the alkali group, with minor grains from 510 m a.s.l. plotted in the X-vacancy group (Fig. 7A). In the Al-Fe-Mg ternary diagram (Henry and Guidotti 1985), tourmaline samples from 510 m a.s.l. plotted in the fields of Li-poor granitoids and associated pegmatites and aplites, or metapelites and metapsammites without an Al-saturated phase (Fig. 7B). Similarly, samples from 830 m a.s.l. were mainly plotted in these two fields, with a few scattered in the fields of Fe^{3+}-rich quartz-tourmaline rocks, calc-silicate rocks, or metapelites and

metapsammites with an Al-saturated phase (Fig. 7B). However, samples from the shallowest 1230 m a.s.l. were mostly plotted in the fields of Fe^{3+}-rich quartz-tourmaline rocks, calc-silicate rocks, and metapelites (Fig. 7B). The Mg/(Mg+Fe), Na/(Na+Ca) values, and X-site vacancies ($X_{\square}$) for the tourmaline samples showed some scatter with depth but were most clearly plotted in the schorl field (Fig. 8).

The tourmaline samples showed varying and poorly defined trends in the binary diagram of Fe vs. Mg (Fig. 9A), suggesting composite substitutions including $FeMg_{-1}$, [(□, Al) $(Na, Mg)_{-1}$], and $FeAl_{-1}$ (e.g., Baksheev et al. 2018; Qiao et al. 2019). In the diagram of Al-$X_{\square}$ vs. R+$X_{\square}$ (Fig. 9B), all samples were plotted parallel to the $FeAl_{-1}$ exchange vector, which implies that Al variations in the tourmaline were dominantly controlled by $FeAl_{-1}$ substitution (Medaris et al. 2003; Henry et al. 2008). The negative correlation between Ca and $X_{\square}$ (Fig. 9C) indicated [(Ca, R, O) $(\square, Al, (OH))_{-1}$] substitution for the investigated tourmaline samples. The correlations decreased for tourmaline from 510 to 1230 m a.s.l., suggesting an increasingly synergistic influence of [(Ca, R) $(Na, Al)_{-1}$] substitution from deep to shallow levels. Besides, the variations of Al (4.73−6.52 a.p.f.u) in these tourmaline samples were larger than that of Ca (0.05–0.48 a.p.f.u), further confirming that other exchange vectors, such as $FeAl_{-1}$ and [(R, OH) $(AlO)_{-1}$] operated to balance the excess Al (Fig. 9D).

For the oscillatory-zoned tourmaline grains at 1230 m a.s.l. (Fig. 10A), the Si, Fe, and Ca concentrations increased from the cores to the rims (Fig. 10B-D). In contrast, the Al, $B_2O_{3cal.}$, and $H_2O_{cal.}$ concentrations were relatively high in the cores and gradually decreased toward the rims (Fig. 10E-G).

Trace elemental compositions

The trace elemental compositions of the tourmaline samples are listed in Supplementary Table A2. The ranges and median values of individual elements are graphically shown in Figure 11. Most trace elements had concentrations ranging from 0.1 to tens of ppm. The highest median concentrations were those of V, Cr, Zn, Ga, and Sr, which varied from several tens to hundreds of ppm. In contrast, the concentrations of Cu, Ge, As, Rb, Y, Zr, Mo, Ag, Cd, Sb, Ba, Hf, Ta, W, Bi, Th, and U were mostly below 1 ppm or even below the detection limits. Numerous trace elements had concentrations that varied over several orders of magnitude, especially V, Cr, Co, Nb, Ta, Pb, Th, and U. Lithium, Co, Sr, Nb, and Sn concentrations in the tourmaline samples gradually increased from 510 to 1230 m a.s.l. In contrast, the Zn, Ta, Pb, Th, and U contents decreased (Figs. 11, 12). Tourmaline samples generally had low REE contents, many of which were below the detection limits (Figs. 11, 12I). The tourmaline samples from 510 m a.s.l. contained higher LREE with negligible HREE. In contrast, tourmaline samples from 830 and 1230 m a.s.l. were enriched in HREE relative to LREE (Supplementary Table A2; Fig. 13). The median REE content of the tourmaline samples decreased from 510 to 1230 m a.s.l. (Figs. 11, 12I).

Boron isotopic compositions

The boron isotopic compositions of the studied tourmaline samples are provided in Supplementary Table A3 and are graphically illustrated in Figure 14. Tourmaline samples from 510 m a.s.l. had a tight $\delta^{11}B$ interval from -11.5 to -9.3‰, with a mean

323 value of -10.3‰ (n = 16). The $\delta^{11}B$ values for tourmaline sampled from 830 m a.s.l.
324 were higher than those from 510 m a.s.l., ranging from -9.9 to -1.5‰ (mean = -5.7‰;
325 n = 64). Tourmaline samples from the shallowest 1230 m a.s.l. were characterized by
326 the most variable boron isotopic compositions, yielding $\delta^{11}B$ values in a range of -8.0
327 to +6.8‰ (-2.8‰; n = 25). Due to the small grain sizes, the internal $\delta^{11}B$ variations
328 within individual tourmaline grains in the 510 m a.s.l. could not be obtained by LA-
329 ICP-MS. The $\delta^{11}B$ values generally decreased from cores to rims for patchy
330 tourmaline grains at 830 m a.s.l. (Fig. 4F) but broadly increased outward for
331 oscillatory-zoned tourmaline grains at 1230 m a.s.l. (Fig. 5F). Collectively, the $\delta^{11}B$
332 values for all tourmaline samples ranged from -11.5 to +6.8‰ (Fig. 14).
333

334 # DISCUSSION

335 ## Tourmaline origin

336 Tourmaline samples from different levels of the Hewan porphyry coexisted
337 spatially with quartz, pyrite, and other alteration minerals, which predominantly
338 formed orbicules or patches that accounted for approximately 1% of the porphyry
339 (Figs. 3–5). Similar tourmaline occurrences and mineral assemblages have been
340 reported in leucocratic granitic rocks elsewhere, such as the Erongo granite in
341 Namibia (Trumbull et al. 2008), the Heemskirk and Pieman Heads granites in western
342 Tasmania, Australia (Hong et al. 2017), and the Pingying granite in South China
343 (Zhao H.D. et al. 2021). Three explanations have been proposed to understand the

genesis of these tourmaline orbicules or patches: (1) formed through post-magmatic metasomatism by external boron-rich fluids (e.g., Rozendaal and Bruwer 1995); (2) direct crystallization from a B-rich granitic melt (e.g., Perugini and Poli 2007); and (3) precipitation from immiscible, aqueous, and boron-rich fluids during the late stages of granite crystallization (e.g., Trumbull et al. 2008; Balen and Petrinec 2011; Drivenes et al. 2015). The tourmaline orbicules and patches in the Hewan porphyry were physically isolated entities that were unrelated to fractures or veins connected to the enveloping wall rocks (Figs. 3–5). As such, we propose that the tourmaline orbicules and patches were not formed by post-magmatic metasomatism of external fluids. The tourmaline crystals and associated quartz in the orbicules commonly grew perpendicular to the matrix of the Hewan porphyry and replaced feldspar in the matrix (Figs. 3–5), suggesting that tourmaline formation occurred later than porphyry crystallization. Furthermore, the tourmaline grains were intimately intergrown with hydrothermal alteration minerals rather than with rock-forming minerals (Figs. 3–5). In addition, quartz contained abundant boiling fluid inclusion assemblages (Figs. 3D, 4D, 5D). These combined lines of evidence indicate that the tourmaline grains in the Hewan porphyry predominantly crystallized from exsolved, immiscible, aqueous, and boron-rich magmatic-hydrothermal fluids. This view was partly supported by the consistent age of Au mineralization and the hosting Hewan porphyry at ca. 140 Ma (Zhang et al. 2017, 2020).

Previous experimental and textural studies have suggested that crystallization may have caused the granitic magma to separate into aluminosilicate melts and

366 hydrosaline fluids (Veksler et al. 2002; Thomas et al. 2003). During the separation
367 process, K, Si, and Al are preferentially partitioned into the aluminosilicate melt,
368 whereas B, Na, and Fe enter the hydrosaline fluid (Veksler and Thomas 2002; Veksler
369 et al. 2002; Thomas et al. 2003). The ubiquitous leucocratic halos surrounding the
370 tourmaline orbicules are generally represented by residual K-, Si-, and Al-rich melts
371 after the separation of the B-, Na-, and Fe-rich fractions. In addition, because of the
372 migration of Al into the aluminosilicate melt, the B-rich hydrosaline fluid is predicted
373 to be Al-deficient (Thomas et al. 2003). The Al required for tourmaline growth
374 generally originates from the metasomatism of adjacent feldspars and accounts for the
375 intimate mineral associations of tourmaline, sericite, chlorite, smectite, and kaolinite,
376 which are the replacement products of feldspar.

377 Although minor tourmaline samples at 830 m a.s.l. occurred as veins, they were
378 isolated in the Hewan porphyry without any connection to the surrounding rocks (Fig.
379 4B). Furthermore, the tourmaline grains in the veins had morphologies, textures,
380 mineral assemblages, and chemical compositions indistinguishable from those in the
381 orbicules (Supplementary Tables A1–A3). These features suggest that the tourmaline
382 crystals in the veins and orbicules shared a similar origin and that they precipitated
383 from an immiscible, hydrosaline, and B-rich fluid during the late evolution of the
384 Hewan porphyry. Similar tourmaline occurrences have been identified in numerous
385 granitoid intrusions in Tasmania, Australia, and South China (Yang et al. 2015; Hong
386 et al. 2020; Zhao K.D. et al. 2021). A likely explanation for the different tourmaline
387 occurrences is that the tourmaline veins formed later than the orbicules/patches, and

388 the associated fractures provided conduits for migration of the B-rich hydrosaline
389 fluids (e.g., Hong et al. 2020). Collectively, the above textural and petrographic
390 observations suggest that the tourmaline samples from different parts of the Hewan
391 porphyry crystallized predominately from the magmatic-hydrothermal fluids.

392 **Records of hydrothermal fluid evolution**

393 Previous studies have shown that the composition of hydrothermal tourmaline is
394 controlled not only by crystallography (e.g., Mark et al. 2013), but also by
395 geochemistry of the fluids (e.g., Jiang et al. 2002, 2008; Slack and Trumbull 2011),
396 chemical composition of the host rocks (e.g., Henry and Guidotti 1985; Su et al.
397 2016), and pressure-temperature conditions (e.g., von Goerne et al. 2001, 2011;
398 Berryman et al. 2015). Therefore, elements with few crystal effects can be used to
399 investigate the associated geological processes that control evolution of the
400 tourmaline chemistry. Major and trace element correlations are commonly used to
401 reveal the dominant factors controlling tourmaline composition (e.g., Mark et al.
402 2013; Zhao H.D. et al. 2019, 2021). In this study, almost all the trace elements (e.g.,
403 Li, Co, Zn, Sr, Sn, Pb, Th, U, and REE) showed no statistical correlations with
404 Fe/(Fe+Mg) (Fig. 12), suggesting that they were controlled by external factors such as
405 fluid composition and local fluid-rock interaction as previously proposed (e.g., Yang
406 et al. 2015; Duchoslav et al. 2017; Kalliomäki et al. 2017).

407 From the deep to shallow parts of the Hewan porphyry, the Fe content of
408 tourmaline increased, whereas the Al content decreased (Fig. 6). Similar Fe and Al
409 variations were observed from the cores to the rims of the oscillatory-zoned

tourmaline grains in the shallowest part of the porphyry (Fig. 10). The variations in Fe and Al concentrations, combined with the $FeAl_{-1}$ exchange vector (Fig. 9) and increasing tourmaline $Fe^{3+}/(Fe^{3+}+Fe^{2+})$ values from deep to shallow parts (Supplementary Table A1), generally suggest an increasing oxygen fugacity from 510 to 1230 m a.s.l. and from cores to rims of the zoned tourmaline grains at 1230 m a.s.l., which could promote the incorporation of Fe into tourmaline (e.g., Zhao H.D. et al. 2021). This gradual increase in oxygen fugacity was presumably induced by the injection of meteoric water, which commonly contains high levels of free oxygen (e.g., Fan et al. 1994; Zhao H.D. et al. 2021). Convective meteoric water could have leached components from the peripheral Archean metamorphosed mafic volcanic rocks and Mesoproterozoic marine sedimentary rocks, resulting in gradually increasing concentrations of MgO, Na_2O, CaO, Li, Co, and Sr for tourmaline samples from 510 to 1230 m a.s.l. and from cores to rims of the zoned tourmaline grains at 1230 m a.s.l. (Figs. 6, 10–12). The changing redox conditions and fluid mixing could also result in the removal of Sn from the hydrothermal fluid (e.g., Henrich 1990; Zhao H.D. et al. 2021), thus increasing the Sn concentration in the tourmaline samples from deep to shallow levels (Fig. 12E). A gradual change was observed in the composition from schorl to dravite for tourmaline samples from the deep to shallow parts of the Hewan porphyry (Fig. 8). This has been experimentally interpreted in terms of the increasing salinity of the source fluids for tourmaline crystallization (von Goerne et al. 2011; Orlando et al. 2017). This salinity increase was likely caused by the contamination of leached materials from Mesoproterozoic marine carbonates and

evaporites through the circulation of meteoric water. Another possibility is that the wall rock contamination added extra Mg, as addressed above, to the hydrothermal system, which could also contribute to the tourmaline compositional shift from schorl to dravite from deep to shallow parts.

In contrast, the median U, Th, REE, Zn, and Pb contents of the tourmaline samples gradually decreased from 510 to 1230 m a.s.l. (Figs. 11, 12). Furthermore, the tourmaline grains sampled from 510 m a.s.l. were enriched in LREE relative to HREE, whereas those from 830 and 1230 m a.s.l. contained lower LREE than HREE (Fig. 13). Tourmaline samples of 510 m a.s.l. yielded chondrite-normalized REE patterns consistent with the host Hewan porphyry (Zhang et al. 2017), which reflect the magmatic fractionation of zircon, monazite, and apatite in the peraluminous melt (e.g., Pettke et al. 2005). Similar REE features have been identified for tourmaline in numerous magmatic-hydrothermal systems (e.g., Jiang et al. 2004; Yang et al. 2015; Duchoslav et al. 2017) and are commonly interpreted to reflect preferential partitioning of LREE into the magmatic-hydrothermal fluids exsolved from peraluminous granitic melts (Reed et al. 2000). This feature partly confirms that the tourmaline grains at 510 m a.s.l. precipitated from the hydrothermal fluid that evolved from the Hewan porphyry. Several processes can explain the above vertical variations of REE concentrations and chondrite-normalized REE patterns of the tourmaline samples: (1) the presence of HREE-rich mineral inclusions in the tourmaline; (2) co-crystallization of LREE-incorporating phases (e.g., garnet, monazite, apatite) during fluid evolution and tourmaline precipitation; (3) fluid-rock interactions or fluid

454 mixing resulting in fractionation of LREE and HREE (e.g., Jiang et al. 2004; Marks et
455 al. 2013; Yang et al. 2015; Harlaux et al. 2020). The first hypothesis is unlikely
456 because significant caution was taken to screen out any contamination from accessory
457 mineral inclusions in the tourmaline during data processing. Furthermore, even if
458 some tiny accessory minerals were hidden below the tourmaline surface, ablating
459 trace amounts of such accessories may significantly increase the HREE content as
460 well as the total REE content (e.g., Jiang et al. 2004; Yang et al. 2015), which is not
461 consistent with the observed decrease in the total REE content from LREE-rich
462 tourmaline to HREE-rich tourmaline (Figs. 12I, 13). The second hypothesis is a likely
463 explanation for the variation in the tourmaline REE patterns because previous studies
464 have revealed the presence of LREE-rich hydrothermal garnet (Zhang et al. 2020).
465 These garnet grains may have sequestered more LREE than HREE during fluid
466 evolution, resulting in tourmaline at shallower levels containing lower REE
467 concentrations and showing relative HREE enrichment. The third hypothesis may also
468 be involved in REE fractionation. In hydrothermal systems, REE can be complexed
469 with various ligands such as Cl^-, CO_3^{2-}, and F^- (e.g., Wood 1990; Bau 1991; Jiang et
470 al. 1997; Migdisov et al. 2016). The LREE complexes are more stable and mobile
471 than HREE complexes, and this difference in stability increases with increasing
472 temperature (Wood 1990; Migdisov et al. 2016). As such, fluid mixing between
473 magmatic-hydrothermal fluid and meteoric water in the shallower parts of the Hewan
474 porphyry, as revealed by the above major-trace elements, would result in the
475 fractionation of HREE compared to the more mobile LREE in the fluid, and

476 subsequent precipitation of HREE-rich tourmaline.

477 The decreasing Zn and Pb concentrations from the deep to shallow parts were
478 consistent with the distribution of the Au grade (Fig. 2), suggesting that sphalerite and
479 galena co-precipitated with Au-bearing pyrite mainly at deep levels, resulting in the
480 gradual depletion of the residual fluid in these elements. This view is consistent with
481 the mineral assemblages described in Section 2. Therefore, the major and trace
482 elemental compositions of the tourmaline indicated that the exsolved magmatic-
483 hydrothermal fluid played a dominant role in the deeper parts of the Hewan porphyry.
484 The fluid migrated upward and gradually mixed with external meteoric water
485 containing materials leached from Archean metamorphic rocks and Mesoproterozoic
486 marine sedimentary rocks at shallower levels. Gold, Pb, and Zn were predominantly
487 deposited in the deeper parts (e.g., 510 and 830 m a.s.l.).

488 **Constraints on the source of ore fluids**

489 Tourmaline samples from the deepest 510 m a.s.l. yielded a tight $\delta^{11}B$ interval
490 from -11.5 to -9.3‰ (Fig. 14A), which is consistent with $\delta^{11}B$ values of the average
491 continental crust (Fig. 14B) and tourmaline formed in magmatic systems (-15 to -5‰;
492 Marschall and Jiang 2011). This boron isotopic comparability suggests that the boron
493 for the tourmaline samples at 510 m a.s.l. was predominately sourced from the Hewan
494 porphyry, which was mainly derived from the lower crust, as demonstrated by the
495 major and trace element geochemistry and Sr-Nd-Pb isotopes (Zhang et al. 2017).
496 Tourmaline samples from 830 and 1230 m a.s.l. yielded higher $\delta^{11}B$ values of -9.9 to -
497 1.5‰ and -8.0 to +6.8‰, respectively (Fig. 14A). The increasing tourmaline $\delta^{11}B$

values from deep to shallow parts were consistent with boron isotopic variations from cores to rims of the oscillatory-zoned tourmaline in the shallowest level (Fig. 5F). These boron isotopic shifts could have been resulted from (1) the fractionation of boron in the ore fluids of a closed system (i.e., phase separation, Rayleigh fractionation) and/or (2) the mixing of boron from multiple reservoirs in an open system (Krienitz et al. 2008; Pal et al. 2010; Trumbull et al. 2013).

Quartz grains intergrown with tourmaline at different levels contained similar fluid inclusion assemblages comprising single-phase liquid, two-phase vapor-liquid, and three-phase halite-bearing fluid inclusions (Figs. 3D, 4D, 5D), suggesting that phase separation occurred during the alteration and mineralization of the Hewan porphyry. Previous studies, however, have shown that $\Delta^{11}B_{vapor\text{-}liquid}$ are very small (<3‰) at temperatures higher than 140°C (Spivack et al. 1990; Leeman et al. 2005; Liebscher et al. 2005), which cannot account for the largely variable boron isotopes observed here (Fig. 14). Nevertheless, this process could be locally responsible for the decreasing $\delta^{11}B$ values from cores to rims within tourmaline grains (e.g., Fig. 4F). Therefore, in this study, we precluded the possibility of phase separation as the dominant control for boron isotopic variation.

Rayleigh fractionation is another significant mechanism that causes boron isotopic shifts in tourmaline. To better evaluate the role of this process in the observed boron isotopic variation, we used model calculations (Fig. 15). The $\Delta^{11}B_{liquid\text{-}tourmalie}$ is 3.8‰ (Meyer et al. 2008) at 300°C, the peak homogenization temperature of fluid inclusions in quartz of the main Au mineralization stage (Lu et al. 2012; Peng et al.

520 2017). The starting $\delta^{11}B$ value of ore fluid (-7.7‰) was calculated using the lowest
521 $\delta^{11}B$ value of tourmaline (-11.5‰) in this study. The model shows that the percentage
522 of initial boron in the residual fluid (F value) should be less than 0.07 for the boron
523 isotopic composition of tourmaline samples at 830 m a.s.l. (Fig. 15). Such an extreme
524 fractionation is geologically unlikely because of the high modal proportion of
525 tourmaline in the samples. In addition, Rayleigh fractionation could not account for
526 the most positive boron isotopic values of the tourmaline samples at the shallowest
527 level (Fig. 15). Therefore, Rayleigh fractionation was neither the major nor only
528 process that caused the observed boron isotopic variation.

529 Collectively, boron mixing from two reservoirs, one with an enrichment of ^{10}B,
530 represented by the Hewan porphyry, and the other by an external reservoir typically
531 enriched in ^{11}B, is the most likely explanation for the observed boron isotopic
532 variation (e.g., Li et al., 2022). The potential reservoirs rich in ^{11}B are rocks/fluids of
533 marine origin, including marine brine, seawater, marine evaporites, and deep-sea
534 carbonates (Fig. 14B). Marine brine and seawater are unlikely because the adjacent
535 paleo oceans closed at least 100 Ma earlier than Au mineralization (e.g., Zhao et al.
536 2005; Zhang et al. 2020; Wu et al. 2021). Mesoproterozoic dolomites and marbles,
537 containing marine evaporites, were locally present in the Yixingzhai Au mine,
538 particularly in the Hewan porphyry (Fig. 1). As such, we propose that boron in the
539 marine sedimentary rocks, presumably leached and incorporated by convective
540 meteoric water, caused the increasing $\delta^{11}B$ values from deep to shallow levels (e.g.,
541 Xavier et al. 2008).

Implications for Au deposition and further exploration

As documented in Section 2, gold in the mineralized Hewan porphyry mainly occurs as native Au or electrum inclusions in pyrite, which are closely associated with alteration minerals such as quartz, sericite, chlorite, and tourmaline. However, the presence of these alteration minerals does not always indicate the location of economic Au ores, which are predominantly distributed between 500 and 1100 m a.s.l. in the Hewan porphyry (Fig. 2). Clarifying the mechanisms of Au precipitation and chemical proxies for economic zones is essential for revealing the genesis of the Au mineralization and for further Au exploration. In magmatic-hydrothermal ore systems, metal precipitation is commonly caused by fluid separation, fluid-rock interactions, and/or fluid mixing (e.g., Williams-Jones and Heinrich 2005; Sillitoe 2010; Fan et al. 2022). As recorded by the quartz fluid inclusion assemblages (Figs. 3D, 4D, 5D), ore-forming fluid separation occurred during Au mineralization and associated alteration from 510 to 1230 m a.s.l. in the Hewan porphyry. However, only the zones between 500 and 1100 m a.s.l. contained large tonnages of high-grade Au ore (Fig. 2), which suggests that fluid separation was not the main mechanism for Au deposition. Nor was fluid-rock interaction the cause of ore deposition because ore-related alteration typically occupies larger spaces than the associated economic Au ores, and not all altered zones are accompanied by economic Au mineralization. The major-trace element and boron isotopic compositions of the tourmaline samples from variable levels of the Hewan porphyry suggest that boron, and other metals and volatiles by inference, were initially sourced from the Hewan porphyry and gradually mixed with

564 meteoric water at shallower levels. As such, we propose that fluid mixing was likely
565 the main mechanism for Au precipitation, although fluid separation and fluid-rock
566 interactions may also locally contribute to the Au deposition. However, external
567 contributions from the Archean metamorphic rocks and Mesoproterozoic marine
568 sedimentary rocks were dominant at 1230 m a.s.l., which decreased with increasing
569 depth to Au-rich 830 and 510 m a.s.l. This observation indicates that a suitable mixing
570 proportion of metal-bearing magmatic-hydrothermal fluid and meteoric water
571 accounted for the Au deposition. However, an accurate proportion could not be
572 determined here and can be evaluated in further studies.

573 From deep to shallow parts of the Hewan porphyry, positive or negative
574 correlations were observed between the $\delta^{11}B$ values and Co, Sr, Pb, and Zn contents
575 of the tourmaline samples (Fig. 16A-D). For example, $\delta^{11}B$ values of the tourmaline
576 and its Co, Sr contents systematically increased, whereas Pb, Zn contents decreased
577 from high-grade Au ores upwards to low-grade or barren zones. These systematic
578 variations, combined with the distribution of Au grade, suggest that tourmaline boron
579 isotopes and trace element compositions could potentially act as proxies for Au
580 exploration. Notably, the tourmaline samples from high-grade ore zones showed $\delta^{11}B$
581 (-11.5–-3.0‰), Co/(Pb+Zn) (<0.01), and Sr/(Pb+Zn) (0.27–1.07) values much lower
582 and more concentrated than those from low-grade or barren zone (-8.0–+6.8‰, 0.01–
583 1.10, 0.15–16.4, respectively; Fig. 16E, F). As discussed above, cobalt and Sr in the
584 tourmaline were predominantly derived from Archean to Mesoproterozoic rocks. In
585 contrast, lead and Zn were mainly sourced from the Hewan porphyry and precipitated

586 with Au. Therefore, the lower and more concentrated $\delta^{11}B$, Co/(Pb+Zn), and
587 Sr/(Pb+Zn) values of tourmaline indicated a dominant magmatic provenance from the
588 Hewan porphyry with minor external contaminations. Such fluids and zones, where
589 tourmaline and pyrite precipitated, were favorable for Au accumulation to form
590 economic ores (e.g., 510 and 830 m a.s.l. in Fig. 2). The increasing and largely
591 scattered values of the three parameters suggested significant contamination from the
592 Archean to Mesoproterozoic rocks by circulating meteoric water, which likely diluted
593 Au and related elements in the ore-forming fluids, resulting in low-grade or even
594 barren zones (e.g., 1230 m a.s.l. in Fig. 2). As such, the tourmaline $\delta^{11}B$, Co/(Pb+Zn),
595 and Sr/(Pb+Zn) values could be useful proxies for exploring similar Au
596 mineralization in the Yixingzhai Au mine. In addition to the mineralized Hewan body,
597 other coeval plutons and cryptoexplosive breccia pipes are also present in the mine
598 (Fig. 1B). Field investigations and independent studies have shown that tourmaline is
599 widespread in these plutons and pipes (e.g., Li and Li 1997; Luo 2009; Li et al. 2014).
600 Therefore, the chemical and isotopic proxies of tourmaline obtained in this study can
601 potentially assist in further Au exploration and evaluation within and around these
602 plutons and pipes.
603

604 ## IMPLICATIONS

605 The chemical and isotopic compositions of tourmaline from the mineralized
606 Hewan porphyry in the Yixingzhai Au deposit can be used to fingerprint ore fluid

607 evolution, reveal the mechanism of metal precipitation, and assist in mineral
608 exploration. Tourmaline in the Hewan porphyry is widely developed from the surface
609 to the deeper parts. Petrographic investigations have shown that tourmaline grains are
610 closely associated with ore and alteration minerals, suggesting a magmatic-
611 hydrothermal origin. This conclusion is further supported by the major-trace element
612 and boron isotope compositions of the tourmaline samples, which indicate that
613 magmatic-hydrothermal fluid was dominant in the deep parts of the Hewan porphyry
614 but gradually mixed with meteoric water in the shallower parts. Suitable mixing of the
615 two fluids results in the formation of Au ores. Tourmaline $\delta^{11}B$, Co/(Pb+Zn), and
616 Sr/(Pb+Zn) values are much lower and more concentrated in the economic Au zones
617 than the low-grade or barren zones, and hence could be useful proxies for exploring
618 similar Au mineralization in and around the Yixingzhai mine area. This study
619 highlights the feasibility of using tourmaline chemical and boron isotopic
620 compositions as vectors for mine-scale mineral exploration.
621

622 **ACKNOWLEDGMENTS**

623 This research was funded by the MOST Special Fund from the GPMR of the
624 China University of Geosciences (Wuhan) (MSFGPMR2022–5). We thank Guo-Ping
625 Wang from the Mineral Exploration Institute, Zijin Mining Group Co., Ltd., and Jie
626 Lin from the GPMR for their assistances during the field investigation and lab
627 analyses. We also thank two anonymous reviewers for their constructive comments,
628 which helped improve the presentation of the manuscript. We extend our gratitude to

Prof. Don R. Baker and Prof. Fang-Zhen Teng for handling the manuscript.

REFERENCES CITED

Arif, M., Henry, D.J., and Moon, C.J. (2010) Cr-bearing tourmaline associated with emerald deposits from Swat, NW Pakistan: Genesis and its exploration significance. American Mineralogist, 95, 799–809.

Baksheev, I.A., Trumbull, R.B., Popov, M.P., Erokhin, Y.V., Kudryavtseva, O.E., Yapaskurt, V.O., Khiller, V.V., Vovna, G.M., and Kiselev, V.I. (2018) Chemical and boron isotopic composition of tourmaline from the Mariinsky emerald deposit, Central Urals, Russia. Mineralium Deposita, 53, 565–583.

Balen, D., and Petrinec, Z. (2011) Contrasting tourmaline types from peraluminous granites: a case study from Moslavačka Gora (Croatia). Mineralogy and Petrology, 102, 117–134.

Bau, M. (1991) Rare-earth element mobility during hydrothermal and metamorphic fluid-rock interaction and the significance of the oxidation state of europium. Chemical Geology, 93, 219–230.

Berryman, E.J., Wunder, B., Wirth, R., Rhede, D., Schettler, G., Franz, G., and Heinrich, W. (2015) An experimental study on K and Na incorporation in dravitic tourmaline and insight into the origin of diamondiferous tourmaline from the Kokchetav Massif, Kazakhstan. Contributions to Mineralogy and Petrology, 169, 28.

Chen, C.F., Liu, X.G., Hu, Z.C., Zong, K.Q., and Liu, Y.S. (2014) In situ analysis of

major and trace element compositions of hydrous silicate minerals by LA-ICP-MS. Earth Science, 39, 525–536 (in Chinese).

Drivenes, K., Larsen, R.B., Müller, A., Sørensen, B.E., Wiedenbeck, M., and Raanes, M.P. (2015) Late-magmatic immiscibility during batholith formation: assessment of B isotopes and trace elements in tourmaline from the Land's End granite, SW England. Contributions to Mineralogy and Petrology, 169, 1–27.

Duchoslav, M., Marks, M.A.W., Drost, K., McCammon, C., Marschall, H.R., Wenzel, T., and Markl, G. (2017) Changes in tourmaline composition during magmatic and hydrothermal processes leading to tin-ore deposition: The Cornubian Batholith, SW England. Ore Geology Reviews, 83, 215–234.

Dutrow, B.L., and Henry, D.J. (2011) Tourmaline: a geologic DVD. Elements. 7, 301–306.

Dyar, M.D., Wiedenbeck, M., Robertson, D., Cross, L.R., Delaney, J.S., Ferguson, K., Francis, C.A., Grew, E.S., Guidotti, C.V., Hervig, R.L., Hughes, J.M., Husler, J., Leeman, W., McGuire, A.V., Rhede, D., Rothe, H., Paul, R.L., Richards, I., and Yates, M. (2001) Reference minerals for the microanalysis of light elements. Geostandards Newsletter, 25, 441–463.

Fan, G.H., Li, J.W., Valley, J.W., Scicchitano, M.R., Brown, P.E., Yang, J.H., Robinson, P.T., Deng, X.D., Wu, Y.F., Li, Z.K., Gao, W.S., Li, S.Y., and Zhao, S.R. (2022) Garnet secondary ion mass spectrometry oxygen isotopes reveal crucial roles of pulsed magmatic fluid and its mixing with meteoric water in lode gold genesis. Proceedings of the National Academy of Sciences, 119,

673 e2116380119.

674 Fan, H.R., Xie, Y.H., Zhao, R., and Wang, Y.L. (1994) Stable isotope geochemistry of
675 rocks and gold deposits in the Xiong'ershan area, western He'nan province.
676 Contributions to Geology and Mineral Resources Research, 9, 54–64 (in
677 Chinese).

678 Harlaux, M., Kouzmanov, K., Gialli, S., Laurent, O., Rielli, A., Dini, A., Chauvet, A.,
679 Menzies, A., Kalinaj, M., and Fontboté, L. (2020) Tourmaline as a tracer of late-
680 magmatic to hydrothermal fluid evolution: The world-class San Rafael tin (-
681 copper) deposit, Peru. Economic Geology, 115, 1665–1697.

682 Harlaux, M., Kouzmanov, K., Gialli, S., Marger, K., Bouvier, A., Baumgartner, L.P.,
683 Rielli, A., Dini, A., Chauvet, A., Kalinaj, M., and Fontboté, L. (2021) Fluid
684 mixing as primary trigger for cassiterite deposition: Evidence from in situ $\delta^{18}O$-
685 $\delta^{11}B$ analysis of tourmaline from the world-class San Rafael tin (-copper)
686 deposit, Peru. Earth and Planetary Science Letters, 563, 116889.

687 He, H. (2014) Enlightenment on geological characteristics and reserve verification of
688 the Yixingzhai gold deposit in Shanxi Province. Huabei Land and Resources. 59,
689 123–125 (in Chinese).

690 Heinrich, C.A. (1990) The chemistry of hydrothermal tin(-tungsten) ore deposition.
691 Economic Geology, 85, 457–481.

692 Henry, D.J., and Guidotti, C.V. (1985) Tourmaline as a petrogenetic indicator mineral-
693 An example from the staurolite-grade metapelites of NW Maine. American
694 mineralogist, 70, 1–15.

695 Henry, D.J., Sun, H., Slack, J.F., and Dutrow, B.L. (2008) Tourmaline in meta-
696 evaporites and highly magnesian rocks: perspectives from Namibian
697 tourmalinites. European Journal of Mineralogy, 20, 889–904.
698 Henry, D.J., Novák, M., Hawthorne, F.C., Ertl, A., Dutrow, B.L., Uher, P., and
699 Pezzotta, F. (2011) Nomenclature of the tourmaline-supergroup minerals.
700 American mineralogist, 96, 895–913.
701 Hong, W., Cooke, D.R., Zhang, L., Fox, N., and Thompson, J. (2017) Tourmaline-rich
702 features in the Heemskirk and Pieman Heads granites from western Tasmania,
703 Australia: Characteristics, origins, and implications for tin mineralization.
704 American mineralogist, 102, 876–899.
705 Hong, W., Fox, N., Cooke, D.R., Zhang, L., and Fayek, M. (2020) B- and O-isotopic
706 compositions of tourmaline constrain late-stage magmatic volatile exsolution in
707 Tasmanian tin-related granite systems. Mineralium Deposita, 55, 63–78.
708 Hu, Z.C., Liu, Y.S., Gao, S., Xiao, S.Q., Zhao, L.S., Günther, D., Li, M., Zhang, W.,
709 and Zong, K.Q. (2012) A “wire” signal smoothing device for laser ablation
710 inductively coupled plasma mass spectrometry analysis. Spectrochimica Acta
711 Part B: Atomic Spectroscopy, 78, 50–57.
712 Jiang, S.Y., and Palmer, M.R. (1998) Boron isotope systematics of tourmaline from
713 granites and pegmatites: A synthesis. European Journal of Mineralogy, 10, 1253–
714 1265.
715 Jiang, S.Y., Palmer, M.R., Peng, Q.M., and Yang, J.H. (1997) Chemical and stable
716 isotopic compositions of Proterozoic metamorphosed evaporites and associated

717 tourmalines from the Houxianyu borate deposit, eastern Liaoning, China.
718 Chemical Geology, 135, 189–211.
719 Jiang, S.Y., Palmer, M.R., and Yeats, C.J. (2002) Chemical and boron isotopic
720 compositions of tourmaline from the Archean Big Bell and Mount Gibson gold
721 deposits, Murchison Province, Yilgarn Craton, Western Australia. Chemical
722 Geology, 188, 229–247.
723 Jiang, S.Y., Yu, J.M., and Lu, J.J. (2004) Trace and rare-earth element geochemistry in
724 tourmaline and cassiterite from the Yunlong tin deposit, Yunnan, China:
725 implication for migmatitic-hydrothermal fluid evolution and ore genesis.
726 Chemical Geology, 209, 193–213.
727 Jiang, S.Y., Radvanec, M., Nakamura, E., Palmer, M., Kobayashi, K., Zhao, H.X., and
728 Zhao, K.D. (2008) Chemical and boron isotopic variations of tourmaline in the
729 Hnilec granite-related hydrothermal system, Slovakia: constraints on magmatic
730 and metamorphic fluid evolution. Lithos, 106, 1–11.
731 Kalliomäki, H., Wagner, T., Fusswinkel, T., and Sakellaris, G. (2017) Major and trace
732 element geochemistry of tourmalines from Archean orogenic gold deposits:
733 Proxies for the origin of gold mineralizing fluids? Ore geology reviews, 91, 906–
734 927.
735 Krienitz, M.S., Trumbull, R.B., Hellmann, A., Kolb, J., Meyer, F.M., and Wiedenbeck,
736 M. (2008) Hydrothermal gold mineralization at the Hira Buddini gold mine,
737 India: constraints on fluid evolution and fluid sources from boron isotopic
738 compositions of tourmaline. Mineralium Deposita, 43, 421–434.

739 Leeman, W.P., Tonarini, S., Pennisi, M., and Ferrara, G. (2005) Boron isotopic
740 variations in fumarolic condensates and thermal waters from Vulcano Island,
741 Italy: Implications for evolution of volcanic fluids. Geochimica et Cosmochimica
742 Acta, 69, 143–163.
743 Li, S.B., and Li, J.J. (1997) Characteristic of metallogenic geochemistry of Yixingzhai
744 gold mine field, Hengshan Mt., Shanxi Province. Progress in Precambrian
745 Research, 20, 1–21 (in Chinese).
746 Li, S.R., Santosh, M., Zhang, H.F., Luo, J.Y., Zhang, J.Q., Li, C.L., Song, J.Y., and
747 Zhang, X.B. (2014) Metallogeny in response to lithospheric thinning and craton
748 destruction: Geochemistry and U-Pb zircon chronology of the Yixingzhai gold
749 deposit, central North China Craton. Ore Geology Reviews, 56, 457–471.
750 Li, W.B., Qiao, X.Y., Zhang, F.H., and Zhang, L.J. (2022) Tourmaline as a potential
751 mineral for exploring porphyry deposits: a case study of the Bilihe gold deposit
752 in Inner Mongolia, China. Mineralium Deposita, 57, 61–82.
753 Liebscher, A., Meixner, A., Romer, R.L., and Heinrich, W. (2005) Liquid-vapor
754 fractionation of boron and boron isotopes: Experimental calibration at 400°C/23
755 MPa to 450°C/42 MPa. Geochimica et Cosmochimica Acta, 69, 5693–5704.
756 Liu, Y.S., Hu, Z.C., Gao, S., Günther, D., Xu, J., Gao, C.G., and Chen, H.H. (2008) In
757 situ analysis of major and trace elements of anhydrous minerals by LA-ICP-MS
758 without applying an internal standard. Chemical Geology, 257, 34–43.
759 Lu, Y.C., Ge, L.S., Shen, W., Wang, Z.H., Guo, X.D., Wang, L., and Zhou, C.F. (2012)
760 Characteristics of fluid inclusions of Yixingzhai gold deposit in Shanxi Province

and their geological significance. Mineral Deposits 31, 83–93 (in Chinese).

Luo, J.Y. (2009) Genetic mineralogy and metallogenic prognosis of Yixingzhai gold deposit in Fanshi County, Shanxi Province, 138 p. Ph.D. thesis, China University of Geosciences (Beijing) (in Chinese).

Marks, M.A.W., Marschall, H.R., Schühle, P., Guth, A., Wenzel, T., Jacob, D.E., Barth, M., and Markl, G. (2013) Trace element systematics of tourmaline in pegmatitic and hydrothermal systems from the Variscan Schwarzwald (Germany): The importance of major element composition, sector zoning, and fluid or melt composition. Chemical Geology, 344, 73–90.

Marschall, H.R., and Jiang, S.Y. (2011) Tourmaline isotopes: No element left behind. Elements, 7, 313-319.

Medaris, L.G., Fournelle, J.H., and Henry, D.J. (2003) Tourmaline-bearing quartz veins in the Baraboo Quartzite, Wisconsin: occurrence and significance of foitite and "oxy-foitite". The Canadian Mineralogist, 41, 749–758.

Mercadier, J., Richard, A., and Cathelineau, M. (2012) Boron-and magnesium-rich marine brines at the origin of giant unconformity-related uranium deposits: $\delta^{11}B$ evidence from Mg-tourmalines. Geology, 40, 231–234.

Meyer, C., Wunder, B., Meixner, A., Romer, R.L., and Heinrich, W. (2008) Boron-isotope fractionation between tourmaline and fluid: an experimental re-investigation. Contributions to Mineralogy and Petrology, 156, 259–267.

Migdisov, A., Williams-Jones, A.E., Brugger, J., and Caporuscio, F.A. (2016) Hydrothermal transport, deposition, and fractionation of the REE: Experimental

783 data and thermodynamic calculations. Chemical Geology, 439, 13–42.

784 Orlando, A., Ruggieri, G., Chiarantini, L., Montegrossi, G., and Rimondi, V. (2017)
785 Experimental investigation of biotite-rich schist reacting with B-bearing fluids at
786 upper crustal conditions and correlated tourmaline formation. Minerals, 7, 155.

787 Pal, D.C., Trumbull, R.B., and Wiedenbeck, M. (2010) Chemical and boron isotope
788 compositions of tourmaline from the Jaduguda U (-Cu-Fe) deposit, Singhbhum
789 shear zone, India: Implications for the sources and evolution of mineralizing
790 fluids. Chemical Geology, 277, 245–260.

791 Peng, N.H., Shao, Y.J., Liu, Z.F., and Wang, C. (2017) Metallogenic mechanism of
792 Yixingzhai gold ore field in Fanshi county, Shanxi province: Evidences from
793 isotopes and fluid inclusion. The Chinese Journal of Nonferrous Metals, 27, 305–
794 317 (in Chinese).

795 Perugini, D., and Poli, G. (2007) Tourmaline nodules from Capo Bianco aplite (Elba
796 Island, Italy): an example of diffusion limited aggregation growth in a magmatic
797 system. Contributions to Mineralogy and Petrology, 153, 493–508.

798 Pettke, T., Audétat, A., Schaltegger, U., and Heinrich, C.A. (2005) Magmatic-to-
799 hydrothermal crystallization in the W-Sn mineralized Mole Granite (NSW,
800 Australia). Chemical Geology, 220, 191–213.

801 Qiao, X.Y., Li, W.B., Zhang, L.J., White, N.C., Zhang, F.H., and Yao, Z.W. (2019)
802 Chemical and boron isotope compositions of tourmaline in the Hadamiao
803 porphyry gold deposit, Inner Mongolia, China. Chemical Geology, 519, 39–55.

804 Reed, M.J., Candela, P.A., and Piccoli, P.M. (2000) The distribution of rare earth

elements between monzogranitic melt and the aqueous volatile phase in experimental investigations at 800 C and 200 MPa. Contributions to Mineralogy and Petrology, 140, 251–262.

Rozendaal, A., and Bruwer, L. (1995) Tourmaline nodules: indicators of hydrothermal alteration and Sn-Zn-(W) mineralization in the Cape Granite Suite, South Africa. Journal of African Earth Sciences, 21, 141–155.

Sciuba, M., Beaudoin, G., and Makvandi, S. (2021) Chemical composition of tourmaline in orogenic gold deposits. Mineralium Deposita, 56, 537–560.

Sillitoe, R.H. (2010) Porphyry copper systems. Economic Geology, 105, 3–41.

Slack, J.F., and Trumbull, R.B. (2011) Tourmaline as a recorder of ore-forming processes. Elements, 7, 321–326.

Spivack, A.J., Berndt, M.E., and Seyfried, W.E. (1990) Boron isotope fractionation during supercritical phase separation. Geochimica et Cosmochimica Acta, 54, 2337–2339.

Su, Z.K., Zhao, X.F., Li, X.C., and Zhou, M.F. (2016) Using elemental and boron isotopic compositions of tourmaline to trace fluid evolutions of IOCG systems: The worldclass Dahongshan Fe Cu deposit in SW China. Chemical Geology, 441, 265–279.

Sun, S.S., and McDonough, W.F. (1989) Chemical and isotopic systematics of oceanic basalts: implications for mantle composition and processes. Geological Society, London, Special Publications, 42, 313–345.

Thomas, R., Förster, H., and Heinrich, W. (2003) The behaviour of boron in a

827 peraluminous granite-pegmatite system and associated hydrothermal solutions: a
828 melt and fluid-inclusion study. Contributions to Mineralogy and Petrology, 144,
829 457–472.
830 Tonarini, S., Pennisi, M., Adorni Braccesi, A., Dini, A., Ferrara, G., Gonfiantini, R.,
831 Wiedenbeck, M., and Gröning, M. (2003) Intercomparison of boron isotope and
832 concentration measurements. Part I: selection, preparation and homogeneity tests
833 of the intercomparison materials. Geostandards Newsletter, 27, 21–39.
834 Trumbull, R.B., Krienitz, M.S., Gottesmann, B., and Wiedenbeck, M. (2008)
835 Chemical and boron-isotope variations in tourmalines from an S-type granite and
836 its source rocks: the Erongo granite and tourmalinites in the Damara Belt,
837 Namibia. Contributions to Mineralogy and Petrology, 155, 1–18.
838 Trumbull, R.B., Beurlen, H., Wiedenbeck, M., and Soares, D.R. (2013) The diversity
839 of B-isotope variations in tourmaline from rare-element pegmatites in the
840 Borborema Province of Brazil. Chemical Geology, 352, 47–62.
841 van Hinsberg, V.J., Henry, D.J., and Dutrow, B.L. (2011) Tourmaline as a petrologic
842 forensic mineral: A unique recorder of its geologic past. Elements, 7, 327–332.
843 Veksler, I.V., and Thomas, R. (2002) An experimental study of B-, P- and F-rich
844 synthetic granite pegmatite at 0.1 and 0.2 GPa. Contributions to Mineralogy and
845 Petrology, 143, 673–683.
846 Veksler, I.V., Dorfman, A.M., Dingwell, D.B., and Zotov, N. (2002) Element
847 partitioning between immiscible borosilicate liquids: a high-temperature
848 centrifuge study. Geochimica et Cosmochimica Acta, 66, 2603–2614.

Vila, T., and Sillitoe, R.H. (1991) Gold-rich porphyry systems in the Maricunga belt, northern Chile. Economic Geology, 86, 1238–1260.

von Goerne, G., Franz, G., and Heinrich, W. (2001) Synthesis of tourmaline solid solutions in the system Na_2O-MgO-Al_2O_3-SiO_2-B_2O_3-H_2O-HCl and the distribution of Na between tourmaline and fluid at 300 to 700 °C and 200 MPa. Contributions to Mineralogy and Petrology, 141, 160–173.

von Goerne, G., Franz, G., and van Hinsberg, V.J. (2011) Experimental determination of Na-Ca distribution between tourmaline and fluid in the system CaO-Na_2O-MgO-Al_2O_3-SiO_2-B_2O_3-H_2O. The Canadian Mineralogist, 49, 137–152.

Wei, C.J. (2018) Paleoproterozoic metamorphism and tectonic evolution in Wutai-Hengshan region, Trans-North China Orogen. Earth Science, 43, 24–43 (in Chinese).

Williams-Jones, A.E., and Heinrich, C.A. (2005) Vapor transport of metals and the formation of magmatic-hydrothermal ore deposits. Economic Geology, 100, 1287–1312.

Wood, S.A. (1990) The aqueous geochemistry of the rare-earth elements and yttrium: 2. Theoretical predictions of speciation in hydrothermal solutions to 350°C at saturation water vapor pressure. Chemical Geology, 88, 99–125.

Wu, D.D., Li, S., Chew, D., Liu, T.Y., and Guo, D.H. (2021) Permian-Triassic magmatic evolution of granitoids from the southeastern Central Asian Orogenic Belt: Implications for accretion leading to collision. Science China Earth Sciences, 64, 788–806.

871 Xavier, R.P., Wiedenbeck, M., Trumbull, R.B., Dreher, A.M., Monteiro, L.V.S.,
872 Rhede, D., de Araujo, C.E.G., and Torresi, I. (2008) Tourmaline B-isotopes
873 fingerprint marine evaporites as the source of high-salinity ore fluids in iron
874 oxide copper-gold deposits, Carajas mineral province (Brazil). Geology, 36,
875 743–746.
876 Yang, S.Y., Jiang, S.Y., Zhao, K.D., Dai, B.Z., and Yang, T. (2015) Tourmaline as a
877 recorder of magmatic-hydrothermal evolution: an in situ major and trace element
878 analysis of tourmaline from the Qitianling batholith, South China. Contributions
879 to Mineralogy and Petrology, 170, 42.
880 Zhai, M.G. (2011) Cratonization and the Ancient North China Continent: A summary
881 and review. Science China Earth Sciences, 54, 1110–1120.
882 Zhang, J.Q., Li, S.R., Santosh, M., Li, Q., Niu, S.D., Li, Z.D., Zhang, X.G., and Jia,
883 L.B. (2015) Timing and origin of Mesozoic magmatism and metallogeny in the
884 Wutai-Hengshan region: Implications for destruction of the North China Craton.
885 Journal of Asian Earth Sciences, 113, 677–694.
886 Zhang, J.Q., Li, S.R., Santosh, M., Niu, S.D., Li, Q., and Lu, J. (2017) The magmatic-
887 hydrothermal mineralization systems of the Yixingzhai and Xinzhuang gold
888 deposits in the central North China Craton. Ore Geology Reviews, 88, 416–435.
889 Zhang, L.Z. (2018) Element geochemistry and age of the altered-porphyry gold
890 mineralization in Yixingzhai gold deposit, Fanshi city, Shanxi Province. Geology
891 and Mineral Resources of South China, 34, 134–141 (in Chinese).
892 Zhang, L.Z., Chen, L., Wang, G.P., Deng, X.D., and Li, J.W. (2020) Garnet U-Pb

dating constraints on the timing of breccia pipes formation and genesis of gold mineralization in Yixingzhai gold deposit, Shanxi province. Earth Science, 45, 108–117 (in Chinese).

Zhao, G.C., Sun, M., Wilde, S.A., and Li, S.Z. (2005) Late Archean to Paleoproterozoic evolution of the North China Craton: key issues revisited. Precambrian Research, 136, 177–202.

Zhao, H.D., Zhao, K.D., Palmer, M.R., and Jiang, S.Y. (2019) In-situ elemental and boron isotopic variations of tourmaline from the Sanfang granite, South China: Insights into magmatic-hydrothermal evolution. Chemical Geology, 504, 190–204.

Zhao, H.D., Zhao, K.D., Palmer, M.R., Jiang, S.Y., and Chen, W. (2021) Magmatic-hydrothermal mineralization processes at the Yidong tin deposit, South China: Insights from in situ chemical and boron isotope changes of tourmaline. Economic Geology, 116, 1625–1647.

Zhao, K.D., Zhang, L.H., Palmer, M.R., Jiang, S.Y., Xu, C., Zhao, H.D., and Chen, W. (2021) Chemical and boron isotopic compositions of tourmaline at the Dachang Sn-polymetallic ore district in South China: Constraints on the origin and evolution of hydrothermal fluids. Mineralium Deposita, 56, 1589–1608.

FIGURE AND TABLE CAPTIONS

Figure 1. (a) The tectonic division of the NCC relative to the Yixingzhai Au deposit (modified from Zhao et al. 2005). **(b)** Geological map of the Yixingzhai Au deposit

915 (modified from Zhang 2018). Abbreviations: TNCO = Trans-North China Orogen.

916 **Figure 2.** Geologic cross section transecting the Hewan porphyry showing the
917 distribution of Au grade (modified from Shanxi Zijin Mining Company Limited
918 2020). Samples collected from 1230 m, 830 m, and 510 m a.s.l. are shown as Tur-
919 1230, Tur-830, and Tur-510, respectively.

920 **Figure 3.** Photographs showing the characteristics of tourmaline present at 510 m
921 a.s.l. of the Hewan porphyry. **(a)** Tourmaline presents in small orbicules and coexists
922 spatially with quartz and pyrite in the porphyry. **(b)** The micrograph shows tourmaline
923 as columns disseminated in quartz aggregates and enclosed by quartz, sericite,
924 chlorite, smectite, and/or feldspar. **(c)** Minerals in orbicule are composed of pyrite,
925 sericite, quartz, and tourmaline. Tourmaline scatters in the mantle or unidirectionally
926 accumulates along rims of the orbicule. **(d)** Quartz intergrown with tourmaline
927 contains spatially coexisted single-phase liquid, two-phase liquid-vapor, and three-
928 phase halite-bearing fluid inclusions. **(e)** The BSE image shows tourmaline exhibiting
929 slightly strip-like texture. Abbreviations: Qz = quartz, Tur = Tourmaline, Py = pyrite,
930 Ser = sericite, Chl = chlorite, Sme = smectite, Fs = feldspar.

931 **Figure 4.** Photographs showing the characteristics of tourmaline from 830 m a.s.l. of
932 the Hewan porphyry. **(a)** Tourmaline, occurring as orbicules/patches, coexists spatially
933 with quartz and pyrite in the altered porphyry. **(b)** Tourmaline-quartz-pyrite vein
934 transecting but tailing out in the altered porphyry. **(c)** The tourmaline-quartz orbicule
935 is enclosed by leucocratic halo that mainly comprises quartz, sericite, chlorite, and

936 smectite. **(d)** Greenish-brown to yellowish-brown tourmaline intergrows with pyrite
937 and quartz. **(e)** Quartz contains tourmaline inclusion and two-phase liquid-vapor and
938 three-phase halite-bearing fluid inclusions. **(f)** Tourmaline is closely associated with
939 pyrite and exhibits patchy zones in the BSE image. The black dots and nearby
940 numbers are locations of boron isotopic analyses and analytical results in per mil.
941 Abbreviations: Qz = quartz, Tur = Tourmaline, Py = pyrite, Ser = sericite, Chl =
942 chlorite, Sme = smectite, Fs = feldspar.

943 **Figure 5.** Photographs showing the characteristics of tourmaline from 1230 m a.s.l. of
944 the Hewan porphyry. **(a)** Tourmaline-quartz orbicules dispersing in the altered
945 porphyry. **(b)** Large tourmaline-quartz orbicule is rimed by leucocratic halo
946 mineralogically dominated by kaolinite, alunite, sericite, quartz, and/or feldspar. **(c)**
947 Euhedral to subhedral tourmaline grains are interstitial with quartz and show
948 yellowish to dark green colors. **(d)** Greenish tourmaline intergrows with quartz. Tiny
949 tourmaline and pyrite inclusions are encapsulated in the quartz growth zones. **(e)**
950 Quartz in the orbicule containing two-phase liquid-vapor fluid inclusions with
951 variable vapor/liquid ratios and halite-bearing three-phase fluid inclusions. **(f)** The
952 BSE image shows well-developed oscillatory zones of the tourmaline. The black dots
953 and nearby numbers are locations of boron isotopic analyses and analytical results in
954 per mil. Abbreviations: Qz = quartz, Tur = Tourmaline, Kln = kaolinite, Aln = alunite,
955 Ser = sericite, Fs = feldspar, Py = pyrite.

956 **Figure 6.** Box-whisker plot showing major elemental composition of tourmaline
957 samples from 510 m (Tur-510), 830 m (Tur-830), and 1230 m (Tur-1230) a.s.l. of the

Hewan porphyry.

Figure 7. (a) Classification of the principal groups of tourmaline samples from 510 m (Tur-510), 830 m (Tur-830), and 1230 m (Tur-1230) a.s.l. of the Hewan porphyry (after Henry et al. 2011). $X_{\square}$ = X-site vacancy. **(b)** Al-Fe-Mg ternary diagram showing tourmaline samples from the three different levels of the Hewan porphyry (after Henry and Guidotti 1985). 1 = Li-rich granitoid pegmatites and aplites, 2 = Li-poor granitoids and their associated pegmatites and aplites, 3 = Fe^{3+}-rich quartz-tourmaline rocks (hydrothermally altered granites), 4 = metapelites and metapsammites with an Al-saturated phase, 5 = metapelites and metapsammites without an Al-saturated phase, 6 = Fe^{3+}-rich quartz-tourmaline rocks, calc-silicate rocks, and metapelites, 7 = low-Ca metaultramafics and Cr, V-rich sediments, 8 = metacarbonates and metapyroxenites.

Figure 8. Plots of Mg/(Mg+Fe) versus Na/(Na+Ca) **(a)** and Mg/(Mg+Fe) versus X-site vacancy ($X_{\square}$) **(b)** of tourmaline samples from 510 m (Tur-510), 830 m (Tur-830), and 1230 m (Tur-1230) a.s.l. of the Hewan porphyry.

Figure 9. Plots of Mg versus Fe **(a)**, Al-$X_{\square}$ versus R+$X_{\square}$ **(b)**, Ca versus $X_{\square}$ **(c)**, and Al versus Ca **(d)** of cation occupancies in tourmaline samples from 510 m (Tur-510), 830 m (Tur-830), and 1230 m (Tur-1230) a.s.l. of the Hewan porphyry. The common exchange vectors are also shown as references. $X_{\square}$ = X-site vacancy, R = Fe+Mg+Mn, a.p.f.u. = atoms per formula.

Figure 10. (a) The BSE image showing the oscillatory-zoned tourmaline from 1230

979 m a.s.l. of the Hewan porphyry. Also shown are the locations of EPMA analyses from
980 core to rim. The analytical results of Si, Fe, Ca, and Al contents, and calculated B_2O_3
981 and H_2O contents against the locations are illustrated in **(b)-(g)**, respectively.

982 **Figure 11.** Box-whisker plot showing trace elemental compositions of tourmaline
983 samples from 510 m (Tur-510), 830 m (Tur-830), and 1230 m (Tur-1230) a.s.l. of the
984 Hewan porphyry.

985 **Figure 12.** Correlation diagrams of Li **(a)**, Co **(b)**, Zn **(c)**, Sr **(d)**, Sn **(e)**, Pb **(f)**, Th **(g)**,
986 U **(h)**, and REE **(i)** contents against Fe/(Mg+Fe) value for tourmaline samples from
987 510 m (Tur-510), 830 m (Tur-830), and 1230 m (Tur-1230) a.s.l. of the Hewan
988 porphyry.

989 **Figure 13.** Chondrite-normalized REE patterns for tourmaline from 1230 m (Tur-
990 1230), 830 m (Tur-830), and 510 m (Tur-510) a.s.l. of the Hewan porphyry. The C1
991 chondrite data is referred from Sun and McDonough (1989).

992 **Figure 14. (a)** Histogram of $\delta^{11}B$ values of tourmaline samples from 510 m (Tur-
993 510), 830 m (Tur-830), and 1230 m (Tur-1230) a.s.l. of the Hewan porphyry. **(b)**
994 Distribution of $\delta^{11}B$ values of several boron reservoirs (Jiang and Palmer 1998;
995 Marschall and Jiang 2011; Mercadier et al. 2012).

996 **Figure 15.** Rayleigh fractionation model on the evolution of tourmaline and
997 equilibrated fluid $\delta^{11}B$ values in the Hewan porphyry. Tourmaline samples from 510
998 m, 830 m, and 1230 m a.s.l. of the Hewan porphyry are termed as Tur-510, Tur-830,
999 and Tur-1230 respectively. See the text for details.

1000 **Figure 16.** Binary plots of Co versus $\delta^{11}B$ **(a)**, Sr versus $\delta^{11}B$ **(b)**, Pb versus $\delta^{11}B$ **(c)**,
1001 Zn versus $\delta^{11}B$ **(d)**, Co/(Pb+Zn) versus $\delta^{11}B$ **(e)**, and Sr/(Pb+Zn) versus $\delta^{11}B$ **(f)** for
1002 tourmaline samples from 510 m (Tur-510), 830 m (Tur-830), and 1230 m (Tur-1230)
1003 a.s.l. of the Hewan porphyry.

1004 **Table 1.** Characteristics of tourmaline in the three different levels of the Hewan
1005 porphyry

1006 **Supplementary Table A1.** EPMA major elemental compositions of tourmaline
1007 samples from three different levels of the Hewan porphyry

1008 **Supplementary Table A2.** LA-ICP-MS trace elemental compositions of tourmaline
1009 samples from three different levels of the Hewan porphyry

1010 **Supplementary Table A3.** LA-MC-ICP-MS boron isotopic composition of
1011 tourmaline samples from three different levels of the Hewan porphyry

Table 1. Characteristics of tourmaline in the three different levels of the Hewan porphyry

	Tur-510[a]	Tur-830[b]	Tur-1230[c]
Type	Tourmaline orbicules (<0.5 cm in diameter)	Tourmaline orbicules/patches (0.5–2 cm in diameter), veins (variable in length and 5–10 cm in width)	Tourmaline orbicules (0.5–4 cm in diameter)
Occurrence	The tourmaline orbicules are disseminated in the porphyry. In the orbicules, tourmaline grains are scattered in the core and mantle with no orientation and unidirectionally accumulated along the rims	The tourmaline orbicules/patches are disseminated in the porphyry, whereas the tourmaline veins transect but tail out in the porphyry. Tourmaline aggregates are occasionally rimmed by leucocratic halos	The tourmaline orbicules are disseminated in the porphyry. Quartz-tourmaline orbicules are commonly rimed by leucocratic halos
Morphology	Euhedral to anhedral columns, 20–200 μm in diameters, light yellow to dark blue in color	Column to lenticle in shape, 100–1000 μm in diameters, yellowish-brown to greenish-brown in color	Euhedral to subhedral, 200–1500 μm in diameters, yellowish green to dark greenish brown in color
Texture	Slightly strip-like textures in BSE images	Patchy zones in BSE images	Well-developed oscillatory zones in BSE images
Mineral association	Pyrite, sericite, quartz, chlorite, smectite, ±feldspar	Quartz, sericite, pyrite, chlorite, smectite, ±feldspar	Quartz, pyrite, sericite, ±feldspar, ±kaolinite, ±alunite

Notes: [a]Tur-510 means tourmaline samples collected from 510 m a.s.l.
[b]Tur-830 means tourmaline samples collected from 830 m a.s.l.
[c]Tur-1230 means tourmaline samples collected from 1230 m a.s.l.

Fig. 1

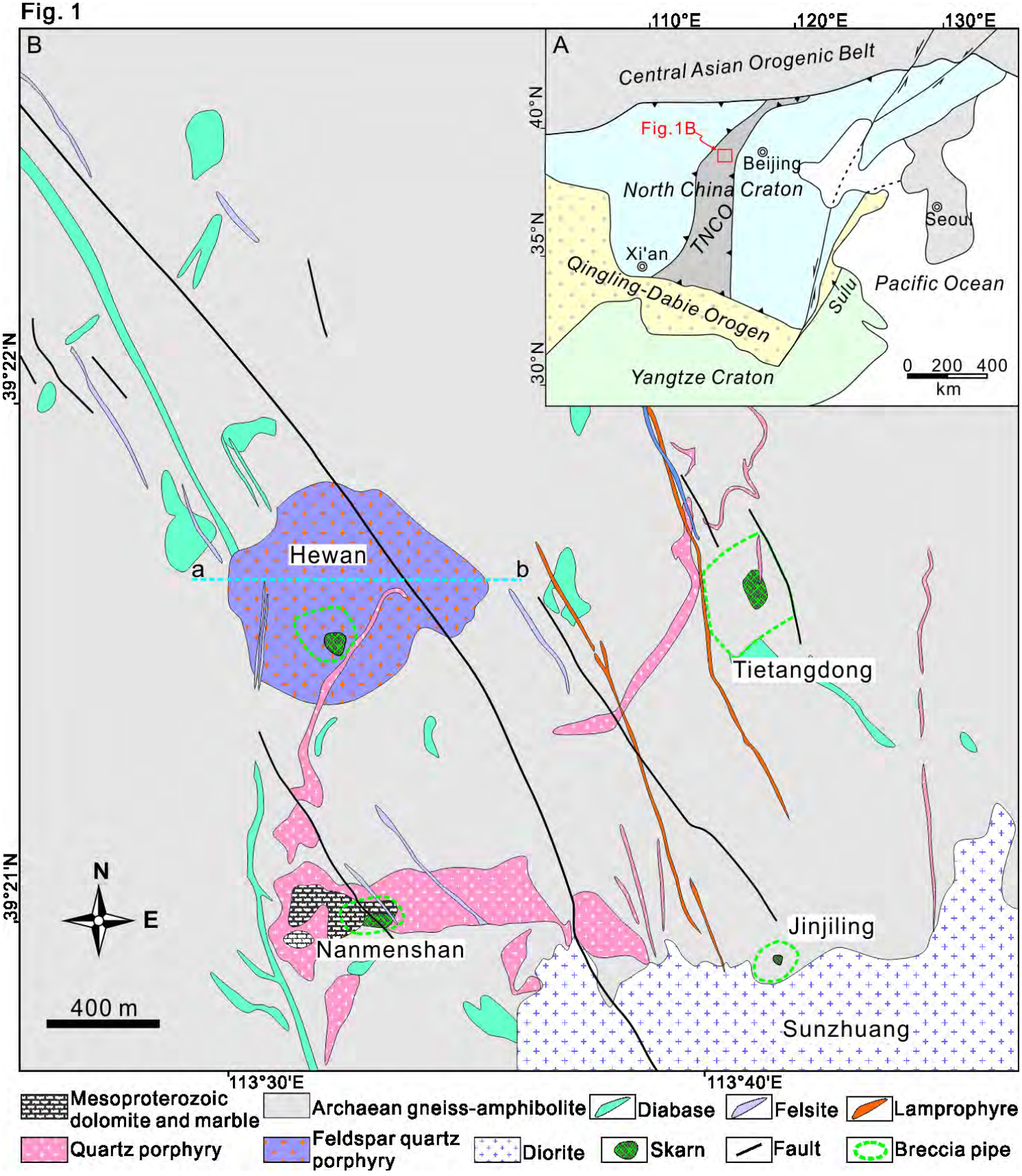
B
A
110°E
120°E
130°E
40°N
35°N
30°N
Central Asian Orogenic Belt
Fig.1B
Beijing
North China Craton
TNCO
Seoul
Xi'an
Qingling-Dabie Orogen
Sulu
Pacific Ocean
Yangtze Craton
0 200 400
km
39°22'N
39°21'N
Hewan
a
b
Tietangdong
Jinjiling
Nanmenshan
Sunzhuang
N
E
400 m
113°30'E
113°40'E
Mesoproterozoic dolomite and marble
Archaean gneiss-amphibolite
Diabase
Felsite
Lamprophyre
Quartz porphyry
Feldspar quartz porphyry
Diorite
Skarn
Fault
Breccia pipe

Fig. 2

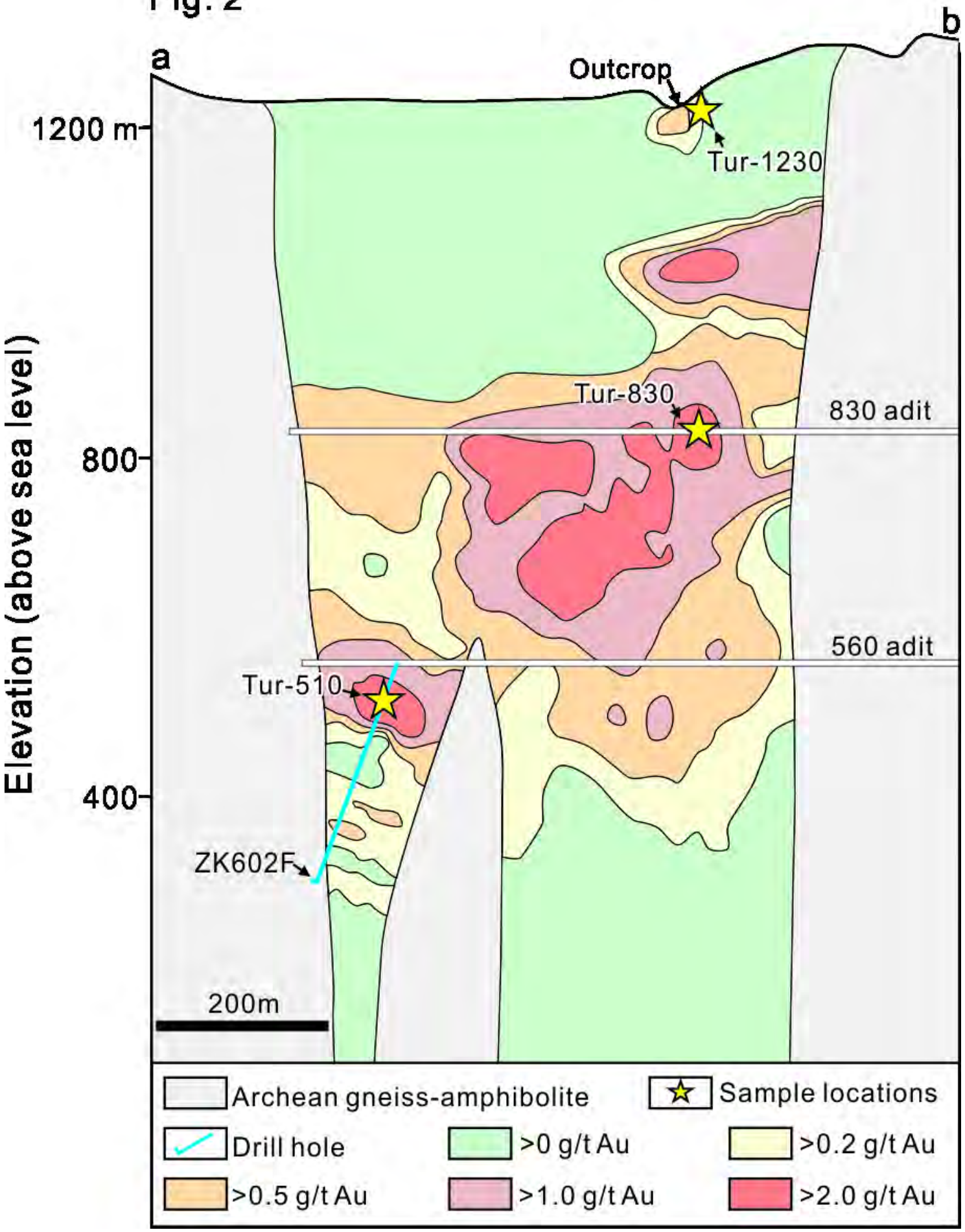
a
b
Outcrop
Tur-1230
1200 m
Tur-830
830 adit
800
560 adit
Tur-510
400
ZK602F
200m
Elevation (above sea level)
Archean gneiss-amphibolite
Sample locations
Drill hole
>0 g/t Au
>0.2 g/t Au
>0.5 g/t Au
>1.0 g/t Au
>2.0 g/t Au

Fig. 3

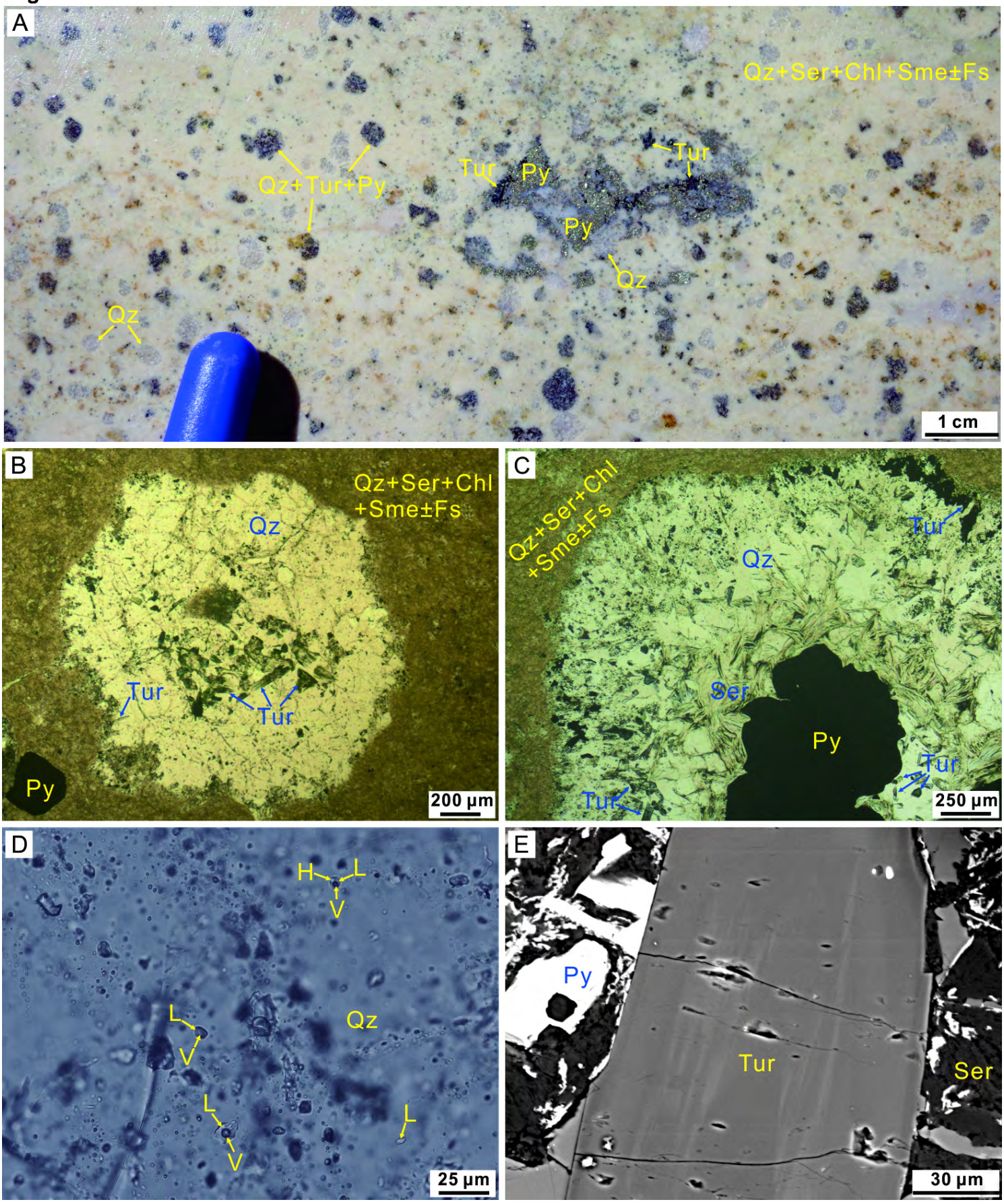
A
Qz+Ser+Chl+Sme±Fs
Qz+Tur+Py
Tur
Py
Tur
Py
Qz
Qz
1 cm
B
Qz+Ser+Chl
+Sme±Fs
Qz
Tur
Tur
Py
200 μm
C
Qz+Ser+Chl
+Sme±Fs
Tur
Qz
Ser
Py
Tur
Tur
250 μm
D
H
L
V
L
V
Qz
L
V
L
25 μm
E
Py
Tur
Ser
30 μm

Fig. 4

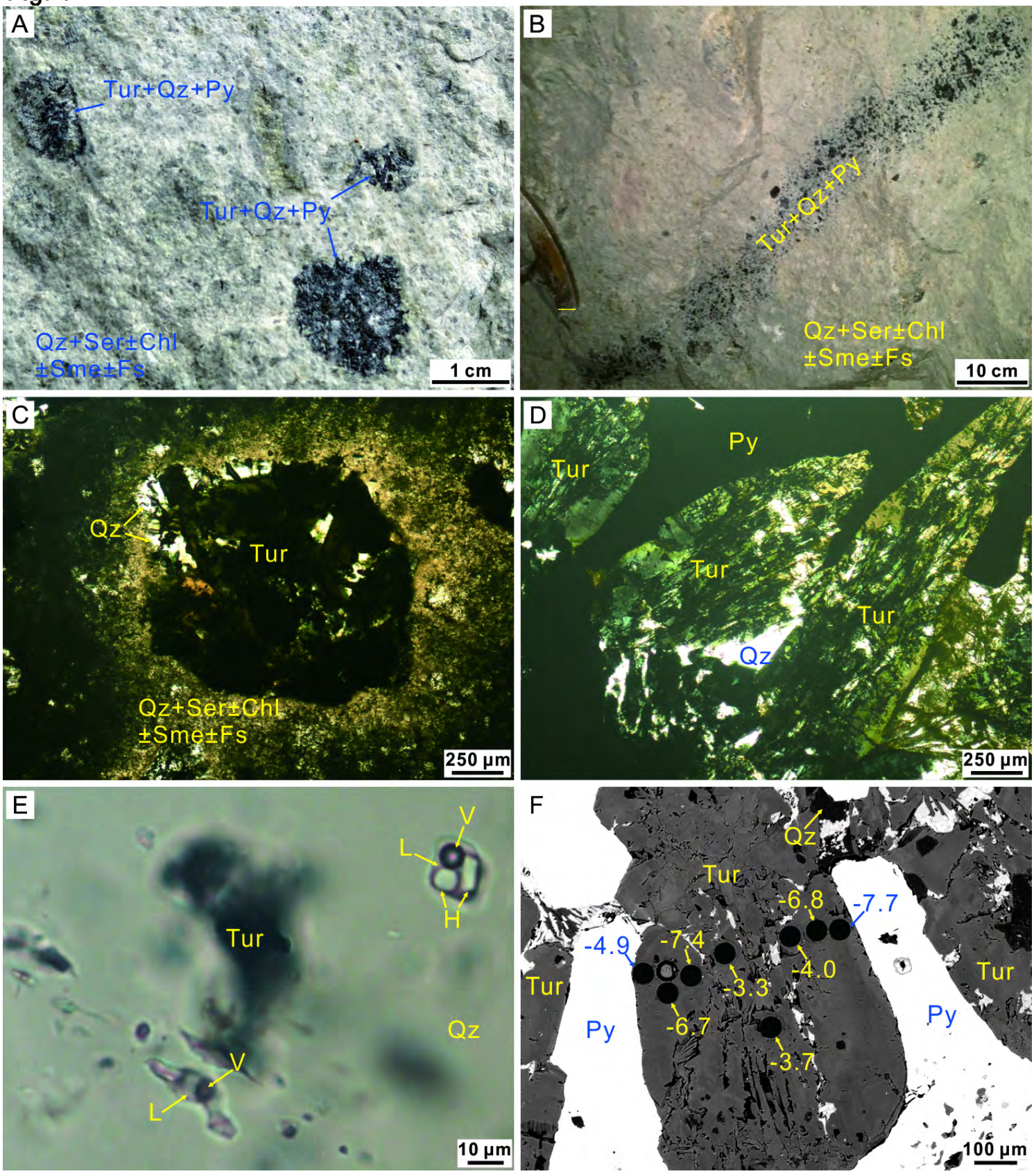
A
Tur+Qz+Py
Tur+Qz+Py
Qz+Ser±Chl
±Sme±Fs
1 cm
B
Tur+Qz+Py
Qz+Ser±Chl
±Sme±Fs
10 cm
C
Qz
Tur
Qz+Ser±Chl
±Sme±Fs
250 μm
D
Py
Tur
Tur
Tur
Qz
250 μm
E
V
L
H
Tur
Qz
V
L
10 μm
F
Qz
Tur
-6.8
-7.7
-4.9
-7.4
-4.0
-3.3
Tur
Tur
Py
-6.7
Py
-3.7
100 μm

Fig. 5

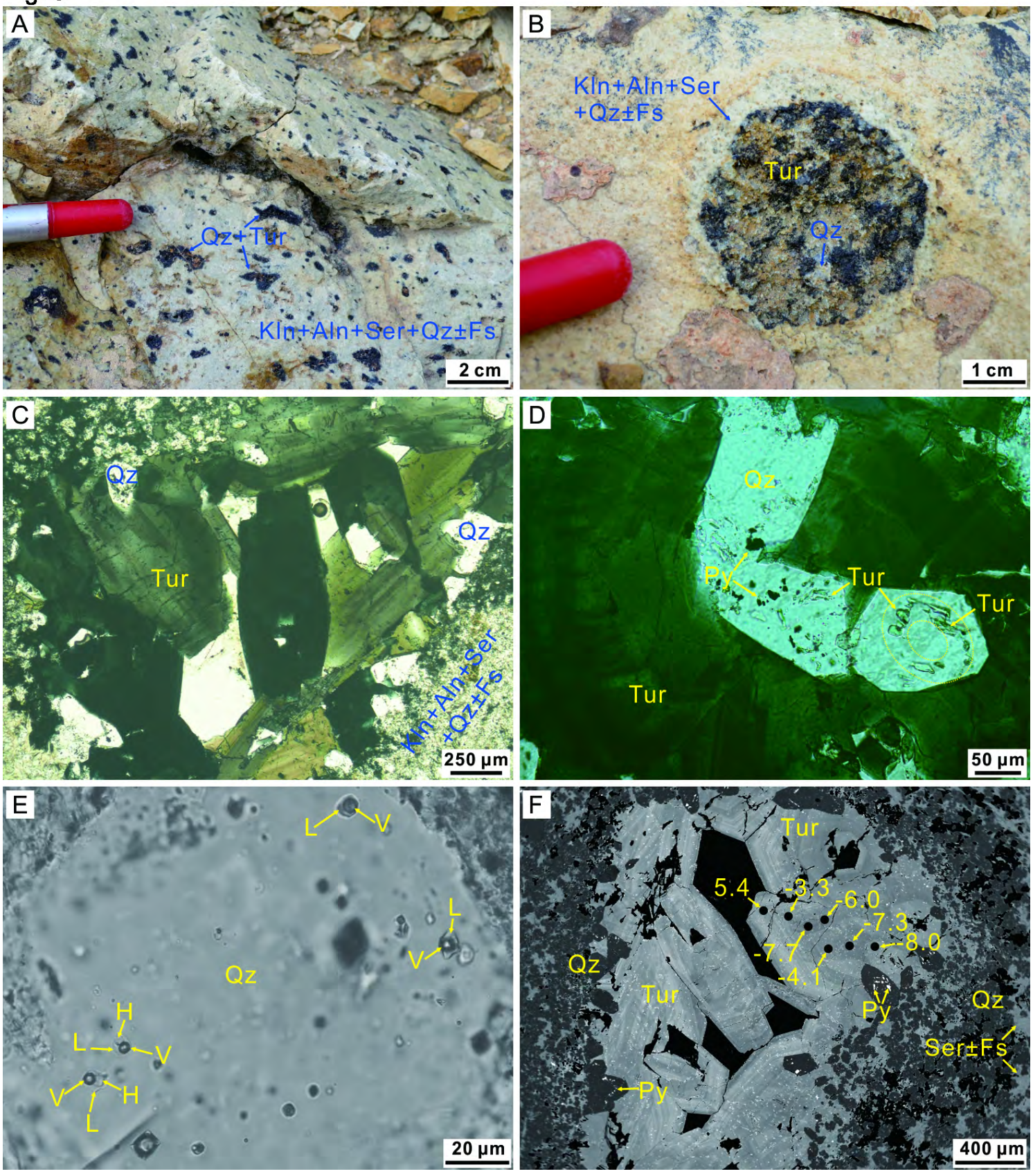
A
Qz+Tur
Kln+Aln+Ser+Qz±Fs
2 cm
B
Kln+Aln+Ser
+Qz±Fs
Tur
Qz
1 cm
C
Qz
Qz
Tur
Kln+Aln+Ser
+Qz±Fs
250 μm
D
Qz
Py
Tur
Tur
Tur
50 μm
E
L
V
L
V
Qz
H
L
V
V
H
L
20 μm
F
Tur
5.4
-3.3
-6.0
-7.3
-8.0
-7.7
-4.1
Qz
Tur
Py
Qz
Ser±Fs
Py
400 μm

Fig. 6

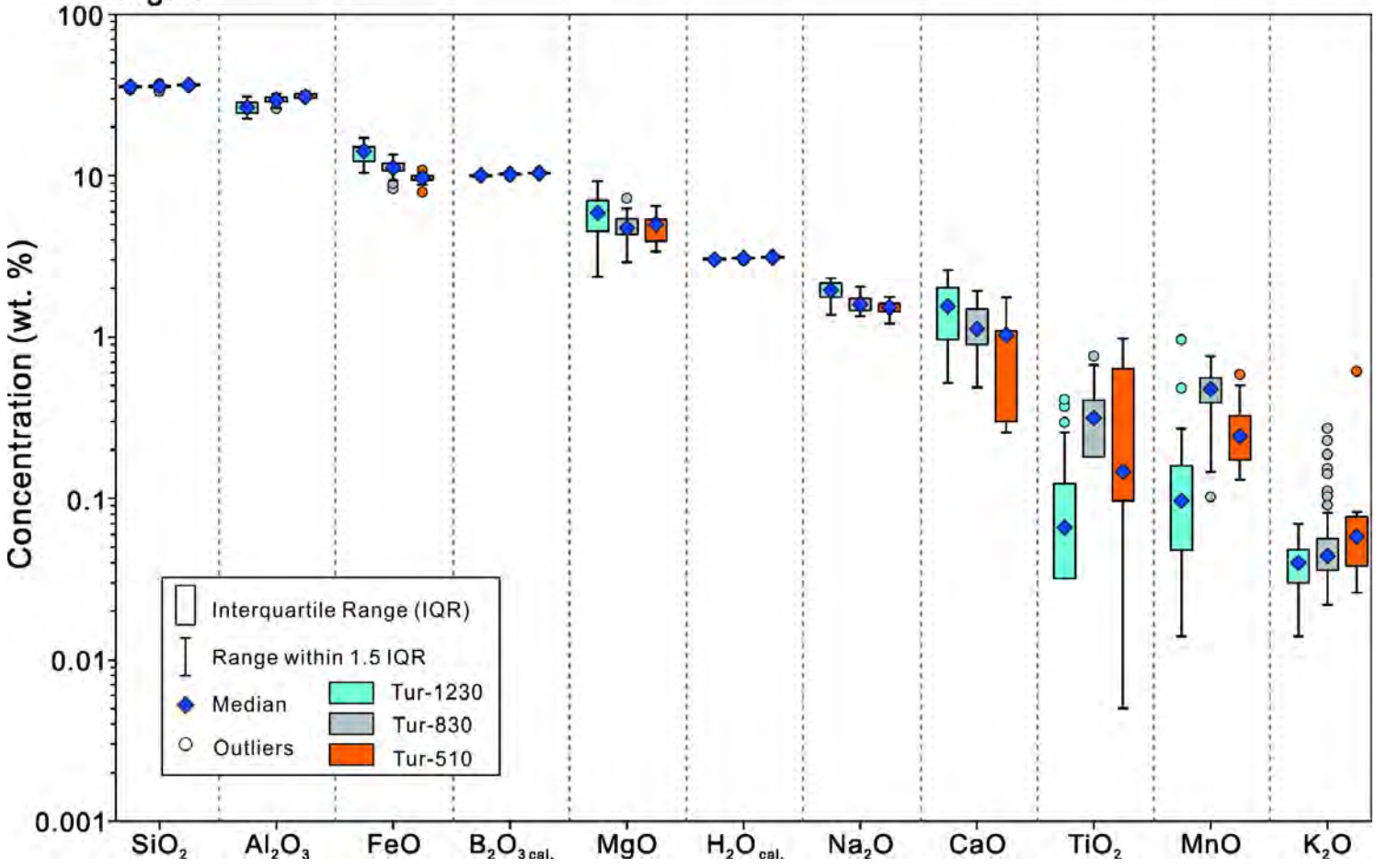
Concentration (wt. %)
100
10
1
0.1
0.01
0.001
Interquartile Range (IQR)
Range within 1.5 IQR
Median
Outliers
Tur-1230
Tur-830
Tur-510
SiO2
Al2O3
FeO
B2O3 cal.
MgO
H2O cal.
Na2O
CaO
TiO2
MnO
K2O

Fig. 7

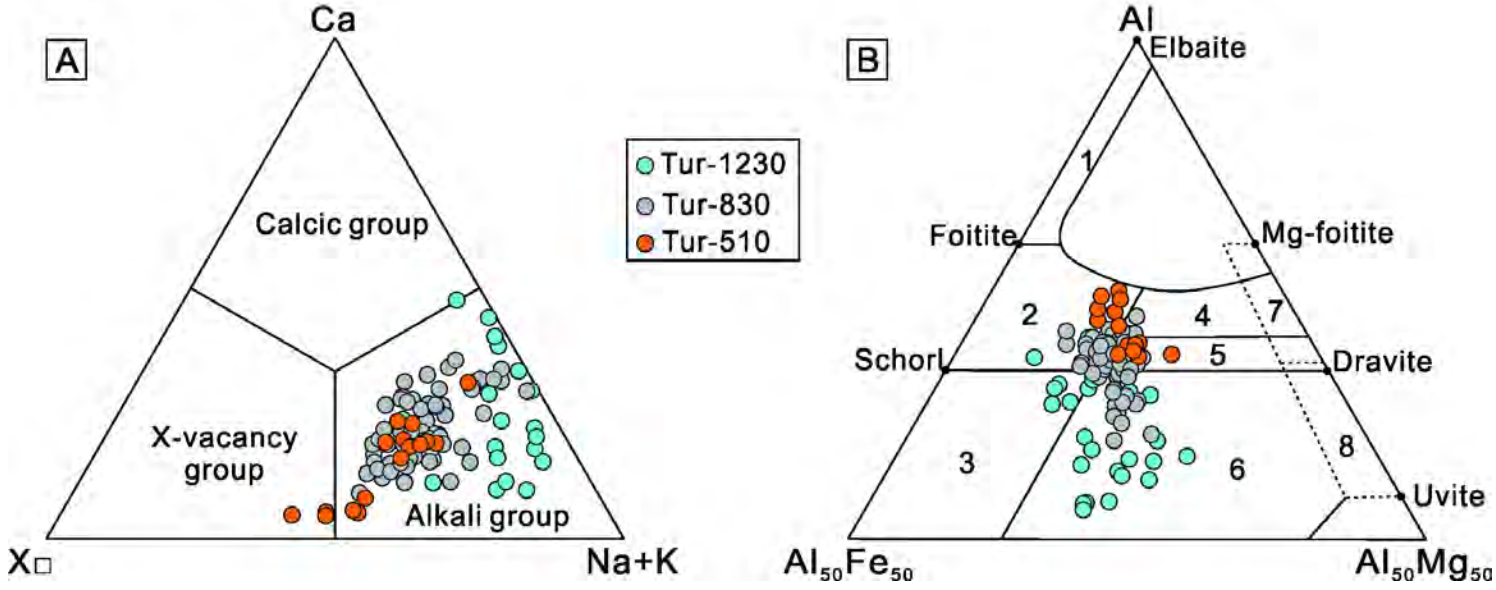
A
Ca
Calcic group
X-vacancy group
Alkali group
X□
Na+K
Tur-1230
Tur-830
Tur-510
B
Al
Elbaite
Foitite
Mg-foitite
Schorl
Dravite
Uvite
1
2
3
4
5
6
7
8
Al50Fe50
Al50Mg50

Fig. 8

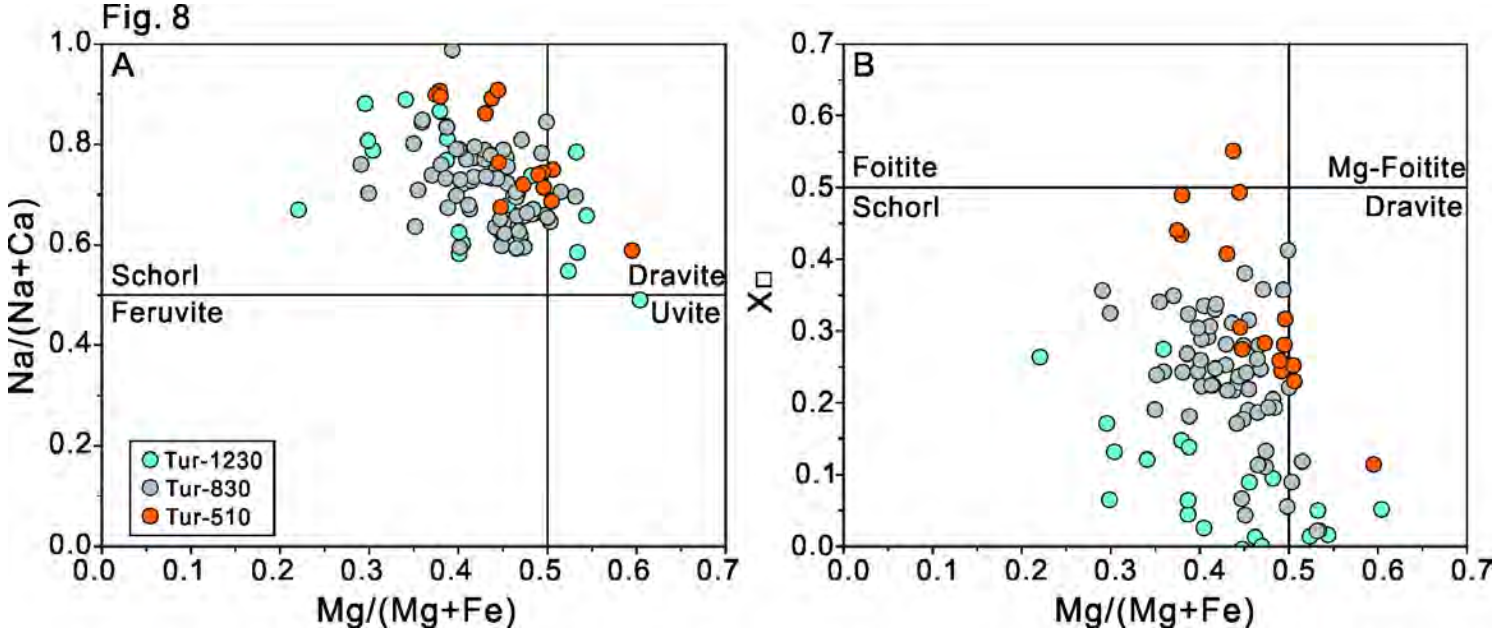
A
Schorl
Feruvite
Dravite
Uvite
Tur-1230
Tur-830
Tur-510
Na/(Na+Ca)
Mg/(Mg+Fe)
B
Foitite
Schorl
Mg-Foitite
Dravite
X□
Mg/(Mg+Fe)

Fig. 9

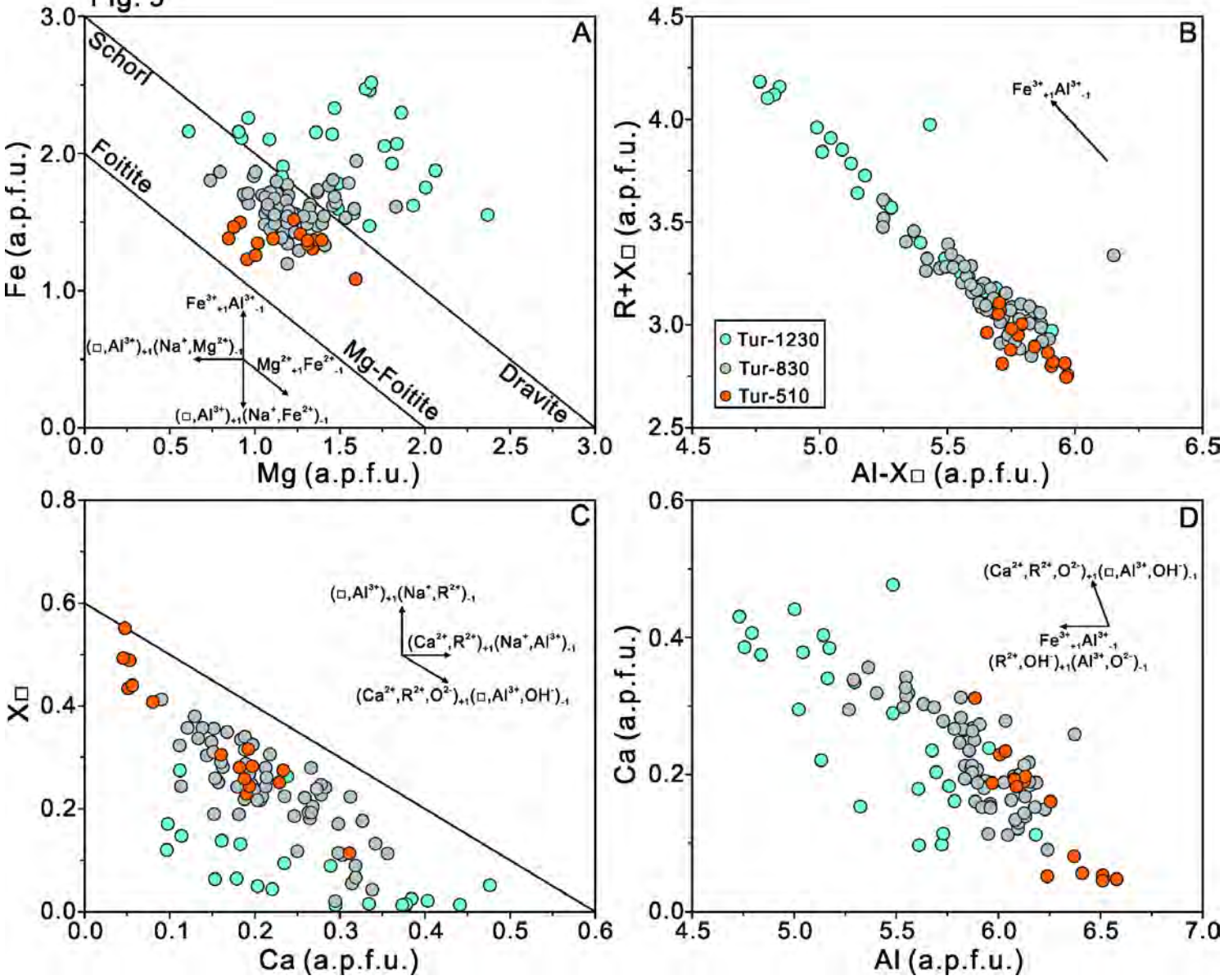
A
Schorl
Foitite
Mg-Foitite
Dravite
Fe (a.p.f.u.)
Mg (a.p.f.u.)
Fe3++1Al3+-1
(□,Al3+)+1(Na+,Mg2+)-1
Mg2++1Fe2+-1
(□,Al3+)+1(Na+,Fe2+)-1
B
R+X□ (a.p.f.u.)
Al-X□ (a.p.f.u.)
Fe3++1Al3+-1
Tur-1230
Tur-830
Tur-510
C
X□
Ca (a.p.f.u.)
(□,Al3+)+1(Na+,R2+)-1
(Ca2+,R2+)+1(Na+,Al3+)-1
(Ca2+,R2+,O2-)+1(□,Al3+,OH-)-1
D
Ca (a.p.f.u.)
Al (a.p.f.u.)
(Ca2+,R2+,O2-)+1(□,Al3+,OH-)-1
Fe3++1Al3+-1
(R2+,OH-)+1(Al3+,O2-)-1

Fig. 10

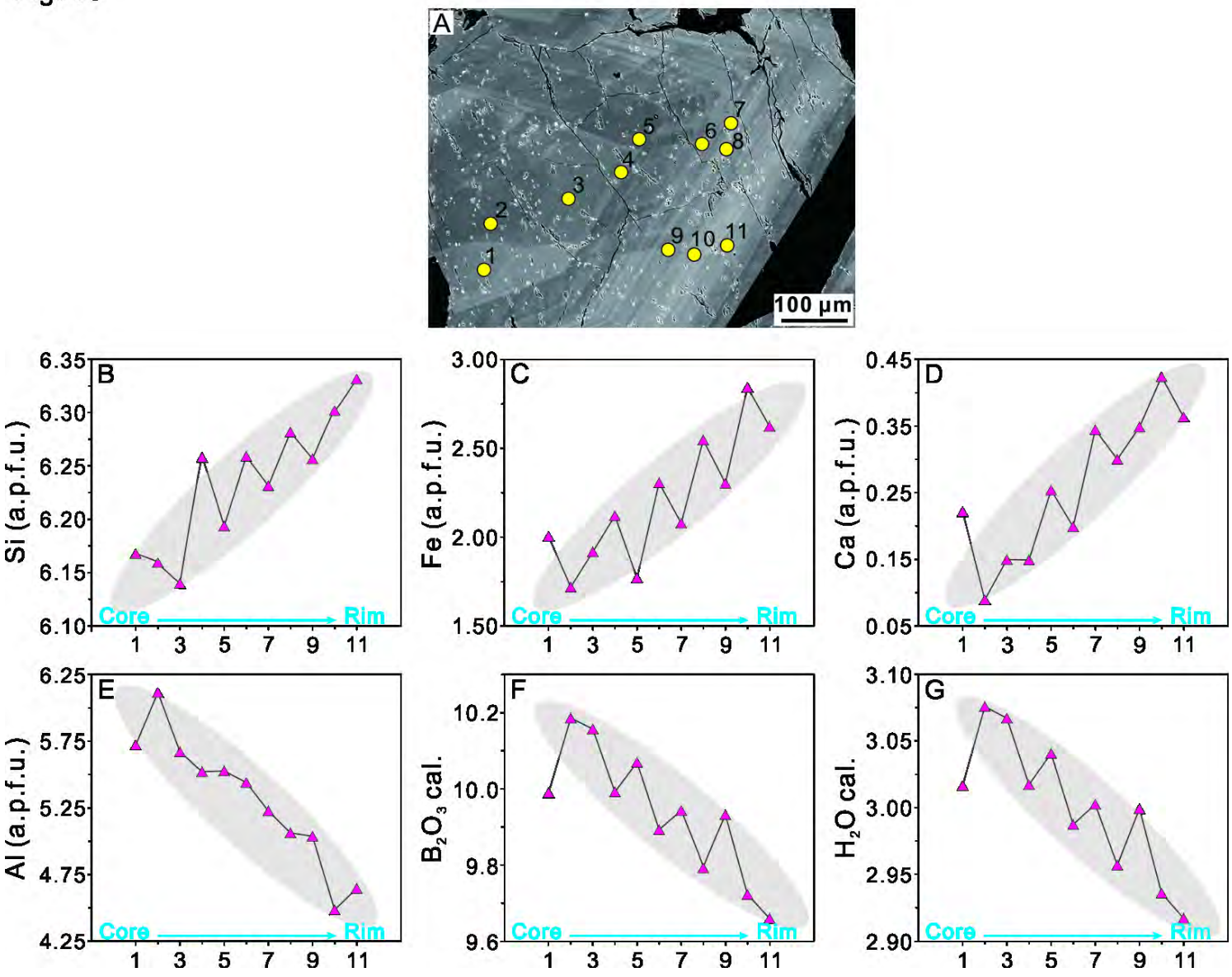
A
1
2
3
4
5
6
7
8
9
10
11
100 μm
B
Si (a.p.f.u.)
6.35
6.30
6.25
6.20
6.15
6.10
C
Fe (a.p.f.u.)
3.00
2.50
2.00
1.50
D
Ca (a.p.f.u.)
0.45
0.35
0.25
0.15
0.05
E
Al (a.p.f.u.)
6.25
5.75
5.25
4.75
4.25
F
B2O3 cal.
10.2
10.0
9.8
9.6
G
H2O cal.
3.10
3.05
3.00
2.95
2.90
Core
Rim
1 3 5 7 9 11

Fig. 11

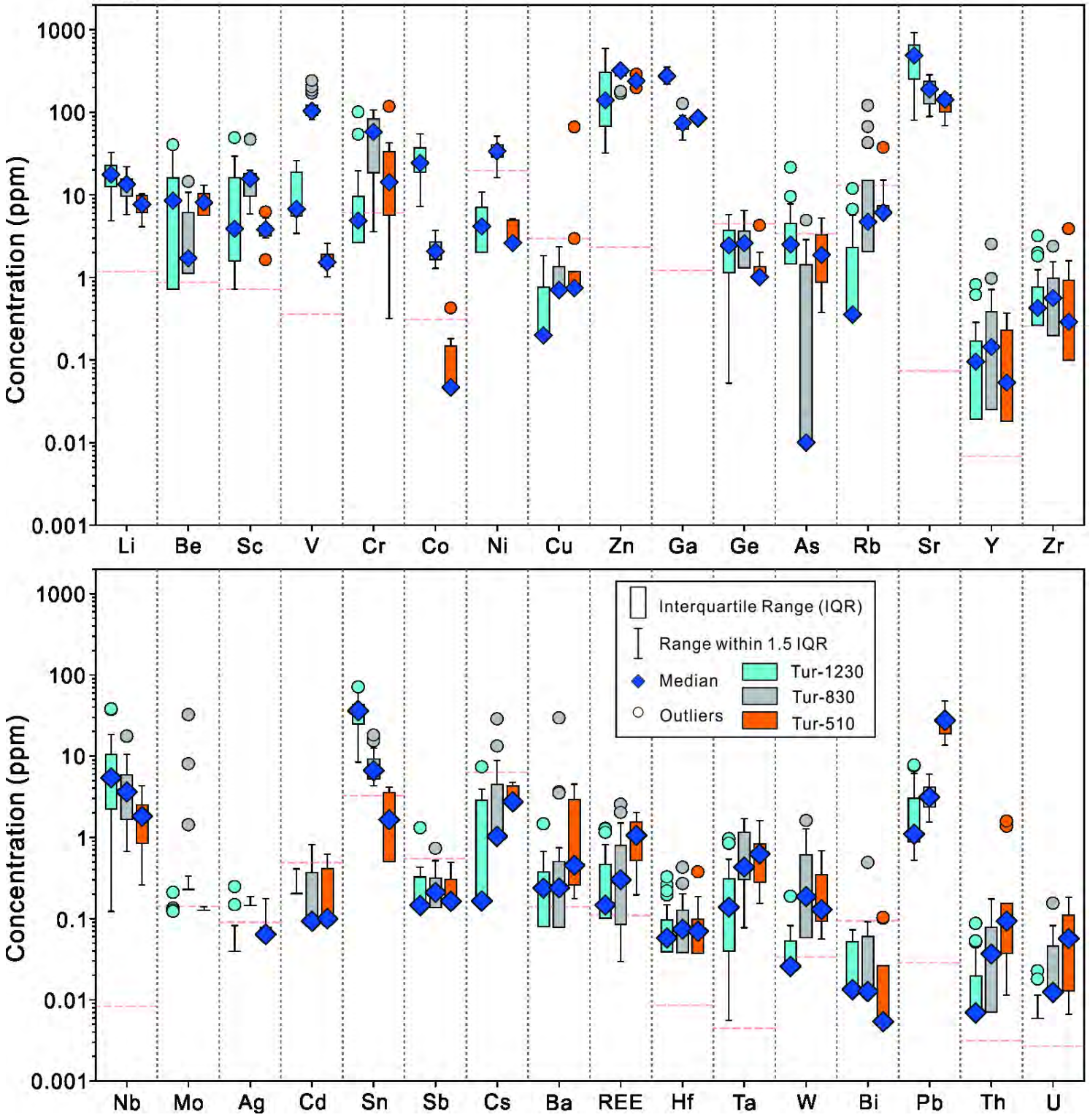
Concentration (ppm)
1000
100
10
1
0.1
0.01
0.001
Li
Be
Sc
V
Cr
Co
Ni
Cu
Zn
Ga
Ge
As
Rb
Sr
Y
Zr
Nb
Mo
Ag
Cd
Sn
Sb
Cs
Ba
REE
Hf
Ta
W
Bi
Pb
Th
U
Interquartile Range (IQR)
Range within 1.5 IQR
Median
Outliers
Tur-1230
Tur-830
Tur-510

Fig. 12

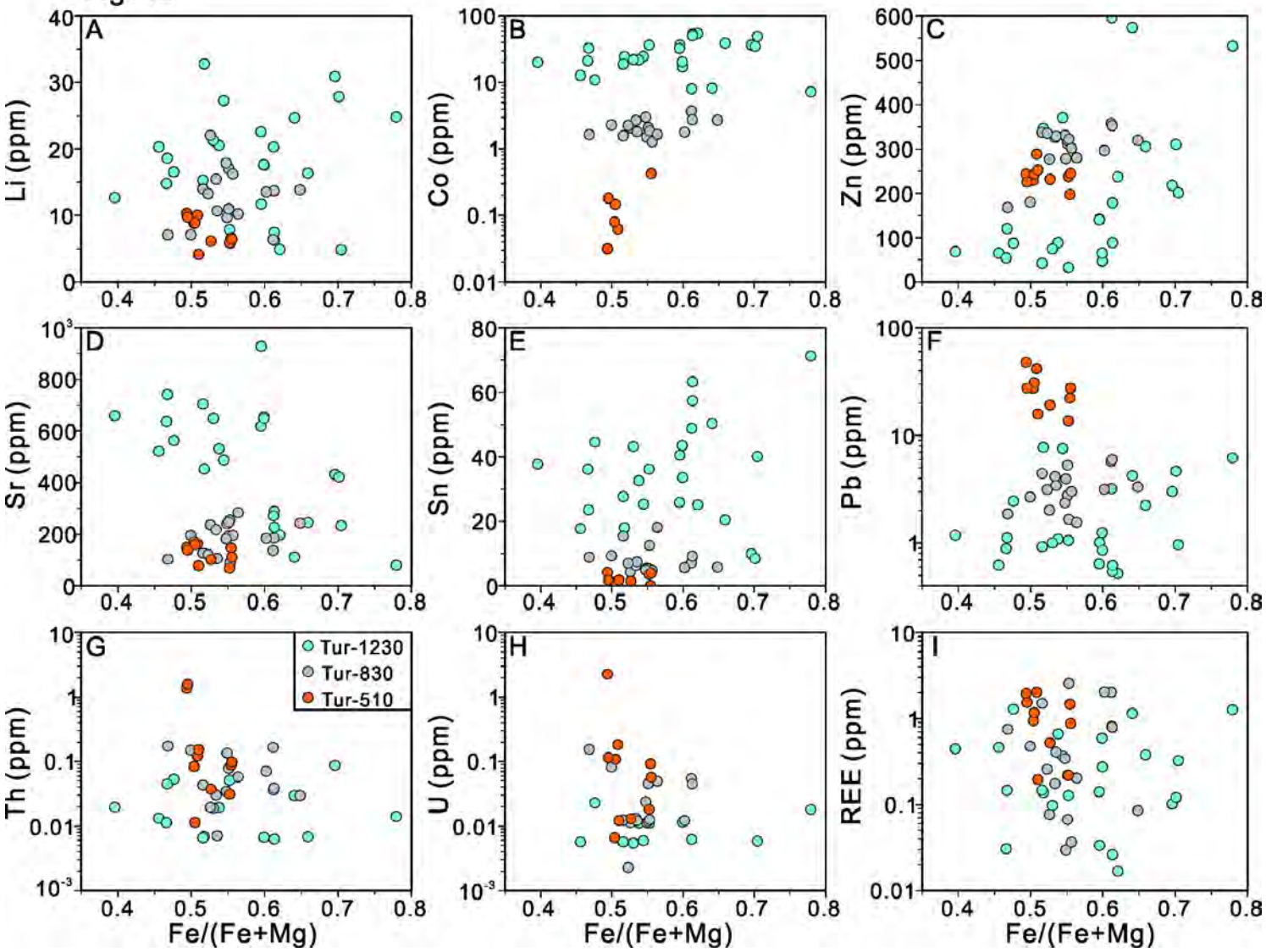
A
B
C
D
E
F
G
H
I
Li (ppm)
Co (ppm)
Zn (ppm)
Sr (ppm)
Sn (ppm)
Pb (ppm)
Th (ppm)
U (ppm)
REE (ppm)
Fe/(Fe+Mg)
Tur-1230
Tur-830
Tur-510

Fig. 13

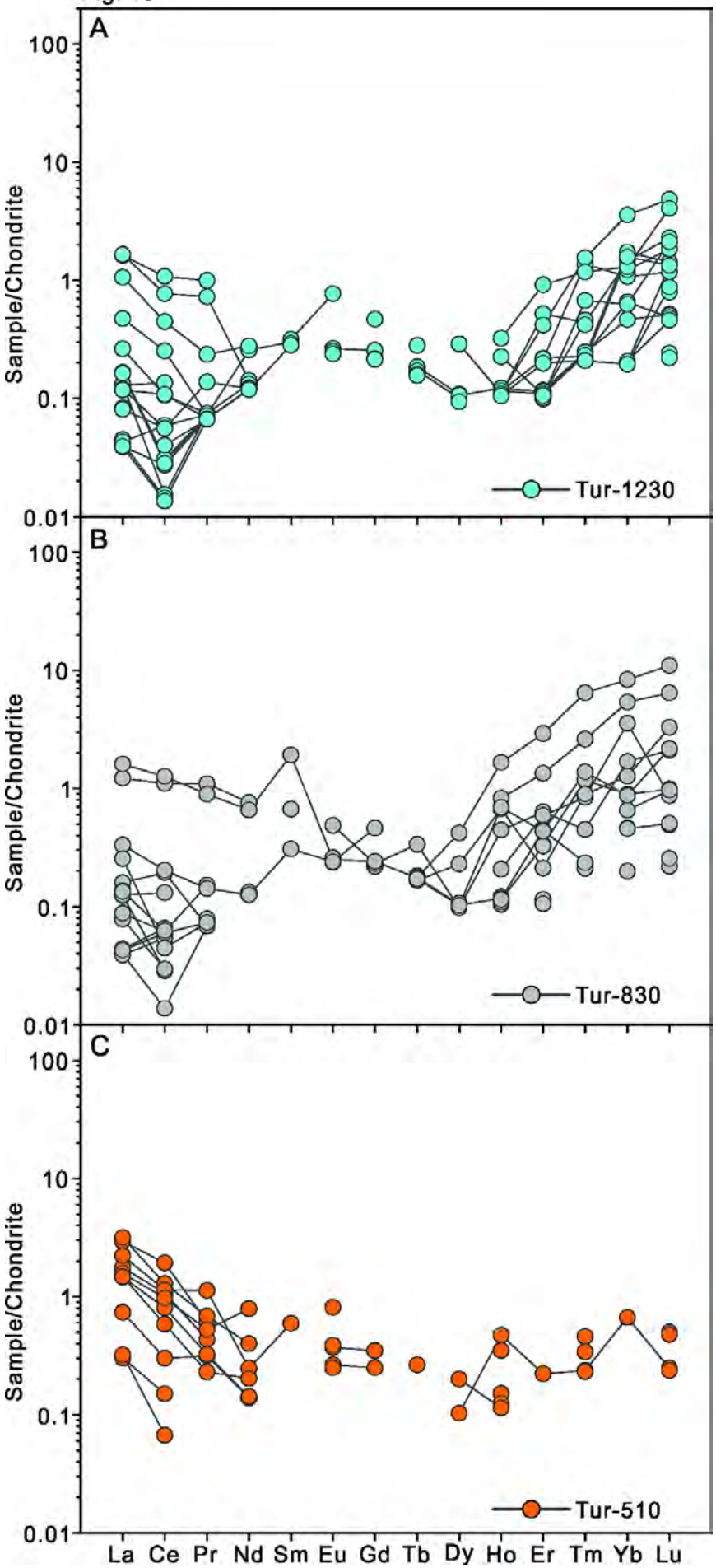
A
B
C
Sample/Chondrite
100
10
1
0.1
0.01
Tur-1230
Tur-830
Tur-510
La Ce Pr Nd Sm Eu Gd Tb Dy Ho Er Tm Yb Lu

Fig. 14

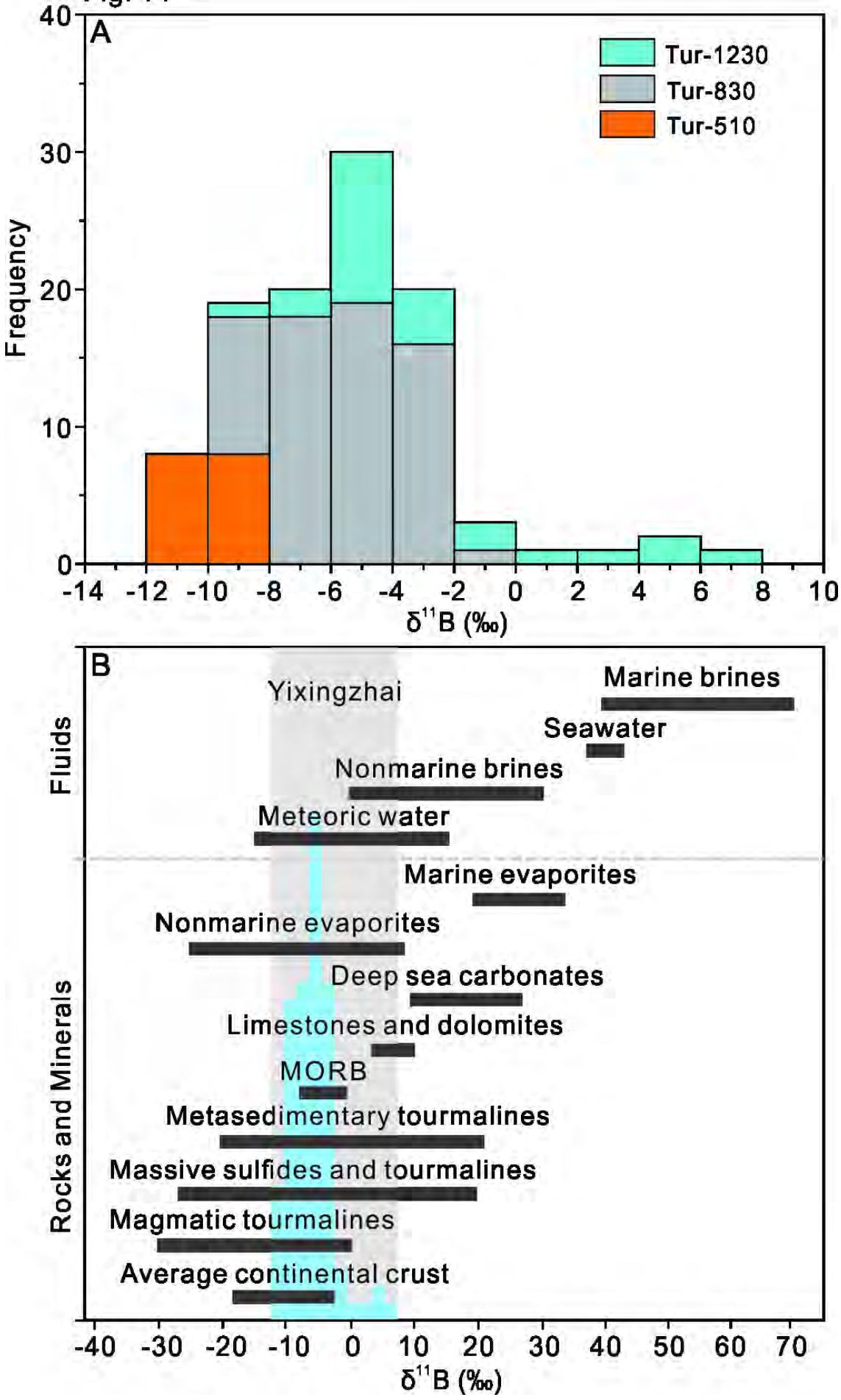
A
Tur-1230
Tur-830
Tur-510
Frequency
40
30
20
10
0
-14 -12 -10 -8 -6 -4 -2 0 2 4 6 8 10
δ11B (‰)
B
Yixingzhai
Marine brines
Seawater
Nonmarine brines
Meteoric water
Fluids
Marine evaporites
Nonmarine evaporites
Deep sea carbonates
Limestones and dolomites
MORB
Metasedimentary tourmalines
Massive sulfides and tourmalines
Magmatic tourmalines
Average continental crust
Rocks and Minerals
-40 -30 -20 -10 0 10 20 30 40 50 60 70
δ11B (‰)

Fig. 15

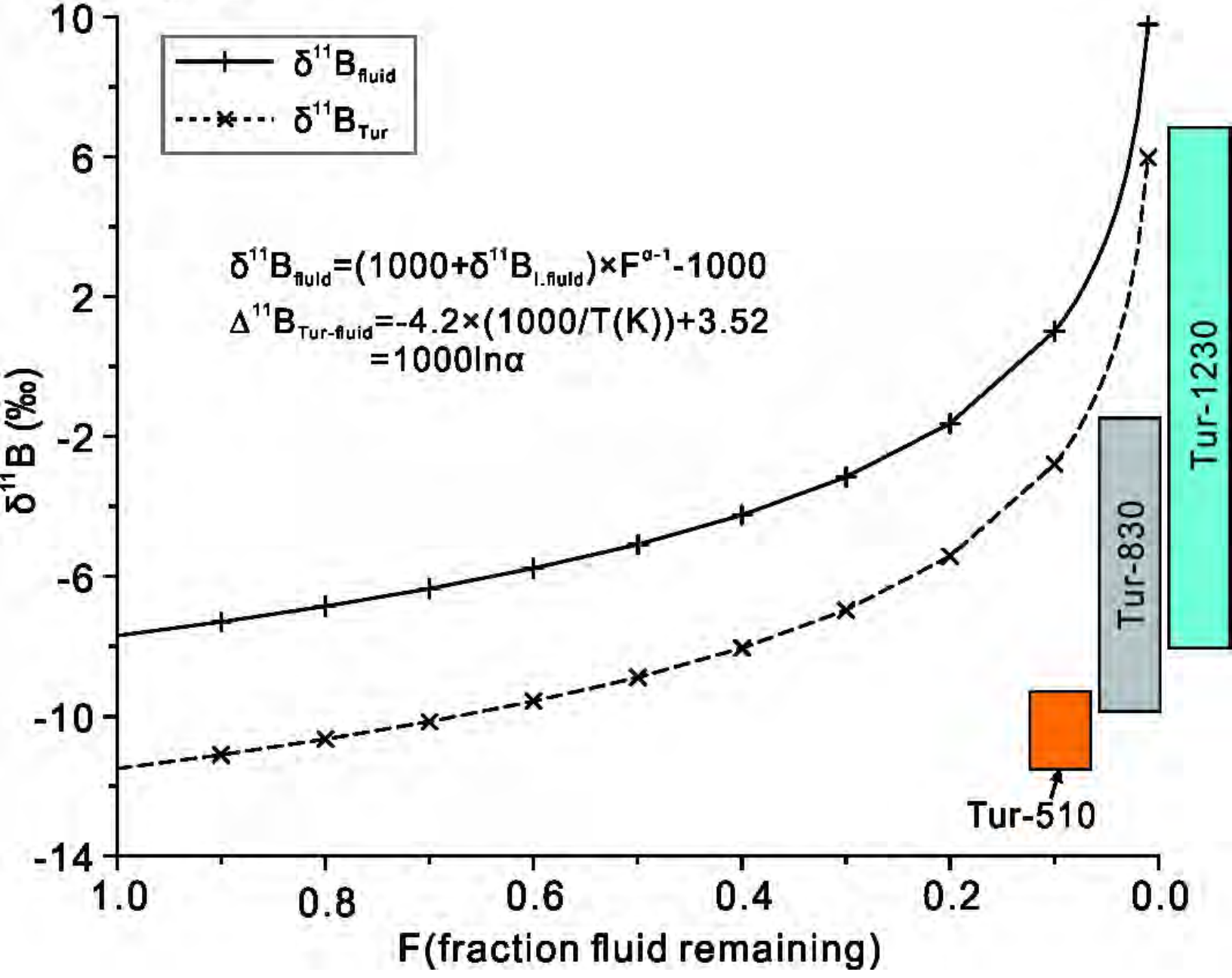
δ11Bfluid
δ11BTur
δ11Bfluid=(1000+δ11Bi.fluid)×Fα-1-1000
Δ11BTur-fluid=-4.2×(1000/T(K))+3.52
=1000lnα
Tur-1230
Tur-830
Tur-510
δ11B (‰)
F(fraction fluid remaining)
10
6
2
-2
-6
-10
-14
1.0
0.8
0.6
0.4
0.2
0.0

Fig. 16

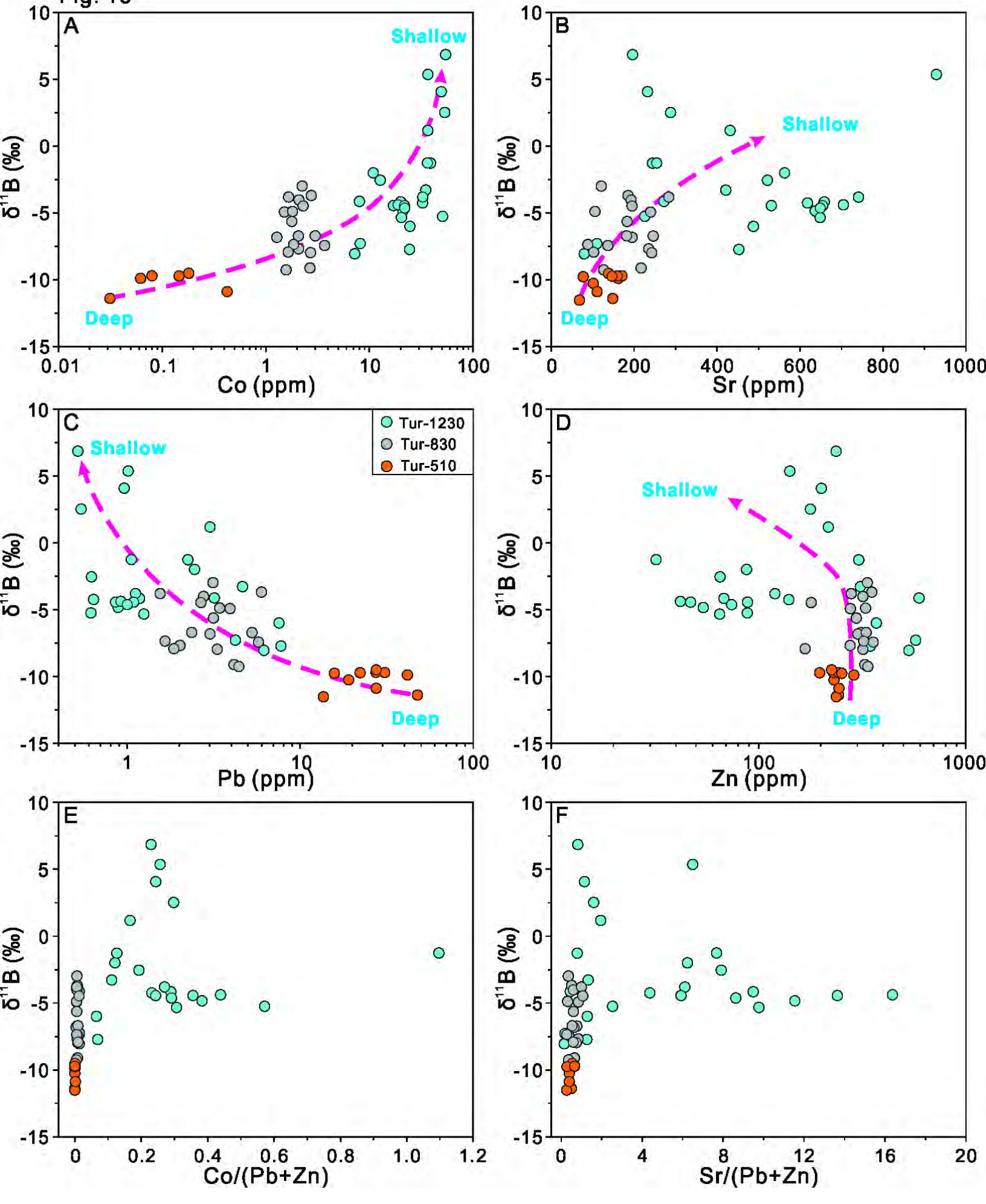
A
Shallow
Deep
δ11B (‰)
Co (ppm)
B
Shallow
Deep
Sr (ppm)
C
Tur-1230
Tur-830
Tur-510
Shallow
Deep
Pb (ppm)
D
Shallow
Deep
Zn (ppm)
E
Co/(Pb+Zn)
F
Sr/(Pb+Zn)